Modelling and Analysis of Compressors in Wet Compression-Resorption Heat Pump Systems Based on Numerical Simulation Using NH_3-H_2O as the Working Fluid

By

Yonghui Wang

Supervisor:

Prof. Kamel Hooman

Master's Dissertation Project

Submitted to the Faculty of Mechanical Engineering / Delft University of Technology
as a partial fulfilment for MSc in Mechanical Engineering

Department of Process & Energy

Tuesday 13th August, 2024

Abstract

The substantial energy consumption driven by industrial and technological advancements, coupled with rapid global economic growth, has led to significant environmental issues, necessitating investment in energy-saving mechanical devices. Compression-resorption heat pumps (CRHPs) are particularly important due to their efficiency across a wide temperature range and superior heat recovery via resorption. The twin-screw compressors in these heat pumps play a critical role, with wet compression often used to manage temperature and prevent overheating through heat transfer from vapor to evaporating water droplets. Understanding the complex turbulent multiphase flows within these compressors requires both experimental and numerical approaches.

This research simplifies the geometry of twin-screw compressors to focus on key features such as suction and discharge fluid domains and screw rotors, omitting external leakage and heat loss due to internal friction. Stationary fluid domains are meshed using Ansys Meshing and Fluent Meshing, and their grid quality and compatibility with Ansys CFX are compared. The narrow and irregular screw domains are meshed in TwinMesh using a "mixed" method, fixing nodes on the female rotor while allowing movement on other curves. The combined meshed domains are then imported into Ansys CFX, where rotational reference frames and boundary conditions are set, preparing for mesh independence studies and flow analysis of both single-phase airflow and ammonia-water multiphase flows to verify the effectiveness of wet compression. Additionally, the influence of gap seals with changeable diameters, which partially recirculates the outlet mass flow back into the suction chamber, on global pressure and mass flow rate is discussed. The simulated results of volumetric efficiency and compressor power consumption are compared with Marina's experimental data to further verify its reliability.

Keywords: Compression-resorption heat pumps; Wet compression; Multi-phase flow; Numerical simulation; Gap seals

Acknowledgements

At the verge of completing the thesis and graduation, I am deeply grateful to all the people who have supported me over the past nine months. First and foremost, I would like to express my sincere appreciation to Prof. Kamel Hooman for giving me the opportunity to conduct research on the complex dynamics of compressor flows. This research has enabled me to learn more than I ever could have in the classroom. I first met Prof. Hooman in March 2023 while taking the course "Mass and Heat Transfer." I quickly discovered that he is a wise and humble mentor, always guiding me in the right direction and genuinely listening to my thoughts. Throughout my thesis, he helped me identify the correct research directions and assisted with obtaining the necessary licenses, significantly boosting the efficiency of my work.

I am also profoundly grateful to my girlfriend, who has been a kind and thoughtful companion throughout this journey. Her unwavering support has given me the confidence to tackle every challenge in the life. I will always cherish the moments we spent together in Delft, Den Haag, Rotterdam, Eindhoven, Utrecht, and Leiden. Without her warm and inspiring presence, I could not have completed this thesis so successfully. I look forward to facing future challenges together, and I will never forget her radiant smile and comforting embrace for as long as I live. In addition, I want to extend my thanks to my friends, with whom I spent many weekends enjoying barbecues, playing video games, or simply exploring different cities. Their advice on managing multiple tasks and avoiding the spread of negative emotions helped me remain cheerful when darkness still looms. I am deeply appreciative of their unwavering support.

Finally, I would like to thank CFX Berlin for providing me with a trial license when I began my meshing work. Their assistance was crucial in solving one of the most difficult problems in meshing and setting up the simulation. Of course, I must also acknowledge my family, who have been my strongest shield. They have shaped me into the person I am today, and their passionate and unwavering care has given me the strength to persevere throughout my life.

Contents

List of Figures

List of Tables

Acronyms

CFD Computational Fluid Dynamics. 11

COP Coefficient of Performance. 3

CPSPR Stagnant Pressure Rise in the Compression Process. 14

CRHP Compression-Resorption Heat Pumps. 3

GVF Gas Void Fraction. 11

GWP Global Warming Potential. 2

HTHP High Temperature Heat Pumps. 2

PR Pressure Ratio. 51

RMS Root Mean Square. 35

RMSE Root Mean Square Error. 36

SESPL Suction Pressure Loss Near the Suction End. 14

SMD Sauter Mean Diameter. 48

SST Shear Stress Transport. 33

STT Share Topology Technique. 22

VCHP Vapor Compression Heat Pumps. 3

Nomenclature

α	Continuous phase
β	Discrete phase
η_{vol}	Volumetric efficiency
γ	Volume fraction
Ω	Rotational speed
Φ	Transported quantity
ψ	Seal mass fraction
φ	Aspect ratio
ϑ	Min angle
P_{comp}	Compressor power consumption
Q_{in}	Inlet mass flow rate
Q_{tot}	Theoretical total volume flow rate

Chapter 1

Introduction

1.1 Research Background

Ever since the beginning of the 21st century, global economic growth has exhibited a clear upward trend [1]. Based on data obtained from the World Bank Group [2], global GDP experienced positive growth throughout the past two decades, with the exceptions of the years 2009 and 2020. These particular years saw economic downturns due to the financial crisis and the COVID-19 pandemic, respectively. Nevertheless, macroeconomic growth is significant, contributing to industrial and technological developments that inevitably consume ample energy and, furthermore, cause environmental problems. For instance, in the year 2012, China accounted for more than half of the world's coal consumption, marking the first time it surpassed this threshold; simultaneously, global coal consumption reached its highest increasing rate among all fossil fuels, increased by 2.5% [3]. In addition, approximately 75% of final energy around the world is utilized to meet heating demands in residential and industrial sectors, and in Netherlands, over 100 PJ of waste energy is produced annually, exacerbating the issues mentioned earlier [4]. These reflect the importance of considering how the efficient utilization of energy from nonrenewable resources can help address and potentially reverse the situation. To address this severe problem, the Paris climate conference was held in December 2015 to discuss the efforts humans should take to limit global warming to well below 2°C

above preindustrial levels [5, 6, 7]. This necessitates the decarbonization of the world economy through both the efficient use and effective recovery of energy. One of many energy-saving mechanical devices that should be shed light on is the heat pump, which can help reduce the use of expensive utilities in industries and make decarbonization a possibility in the industrial production process [8, 9].

Heat pumps have been widely used in combination with distillation columns to achieve energy saving in the process industry [10, 11, 12, 13]. Mix et al.[14] calculated that the energy consumption during distillation processes accounts for approximately 60% of the total energy used in the chemical and petrochemical industries, while the thermodynamic efficiency of the single column is only about 12% for crude distillation [15]. On one hand, the single column requires a large amount of high-quality energy input to satisfy the separation conditions; on the other hand, a similar amount of low-quality waste heat is rejected into the environment. In this case, the integration of distillation columns and heat pumps can help reduce energy consumption based on the fact that heat pumps are devices that recover low-quality waste heat and upgrade it to a higher temperature range for further use. In addition, the pulp and paper, food, and beverage industries are in demand for high-temperature heat pumps as well, since large quantities of heat up to 200°C need to be supplied constantly there [16]. Reviewing these points, heat pump systems appear indispensable in industrial processes due to their characteristics of energy efficiency, environmental friendliness, and reduced reliance on fossil fuels. However, the actual use of heat pumps in the industry isn't as widespread as hoped, mainly because of their long payback periods, as stated by the International Energy Agency [17]. In recent years, numerous researchers have conducted extensive studies to investigate how the performance of heat pumps can be enhanced to counteract negative factors such as the long payback period and space requirements. And they mainly focused on the investigation of alternative low global warming potential (GWP) refrigerants, cascade systems and multi-stage cycles, liquid injection and wet compression technology [18]. Arpagaus et al. reviewed the state-of-the-art development of high temperature heat pumps (HTHP) and concluded how coefficient of

performance (COP) of various industrial HTHP change as a function of the temperature lift, as shown in Figure 1.1 [19]. Xiaohui et al. utilized a near-azeotropic refrigerant mixture called BY-4 to verify its feasibility and reliability as a working fluid for HTHP [20], while Zhang et al. employed BY-5 as the refrigerant to demonstrate its capability to generate heat at a temperature of 135°C with good performance in HTHP [21].

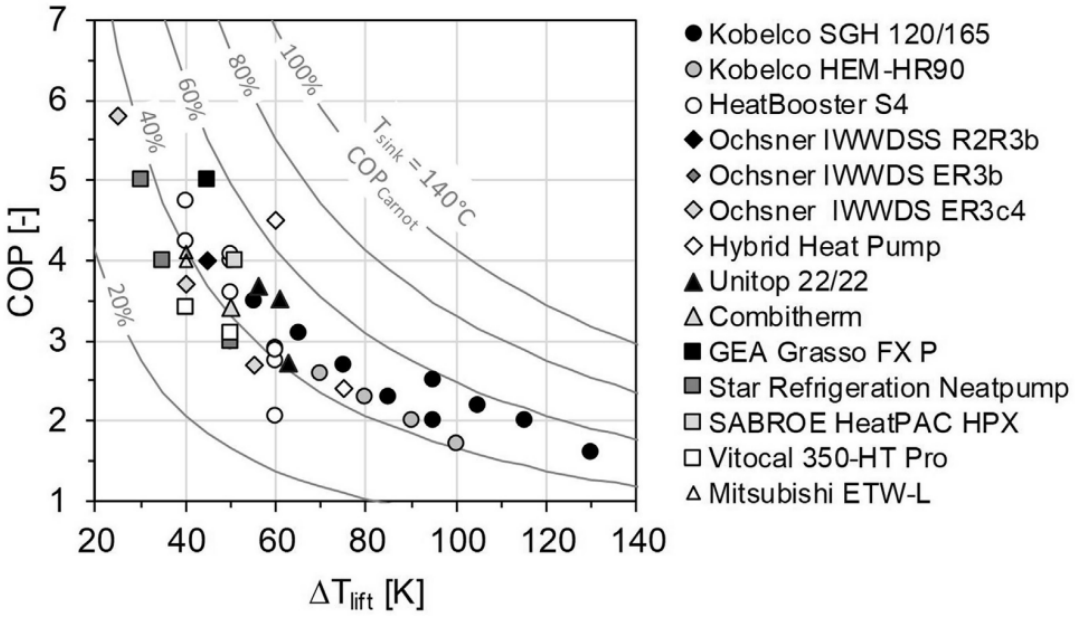

Figure 1.1: COP change as a function of the temperature lift in various industrial HTHP. Data from Arpagaus et al. (2018).

Among all the research related to the performance of heat pump cycles, vapor compression heat pumps (VCHP) and compression-resorption heat pumps (CRHP) are of the most interest. Refrigerants inside classic VCHP typically undergo four stages, with phase changes happening in condensers and evaporators. VCHP utilize dry compression to compress refrigerants from the saturated vapor state to the superheating state, during which the pressure, temperature, and internal energy of refrigerants increase, preparing well for efficient heat transfer during the subsequent condensation stage. In some cases, when there is a temperature glide of the heat sink/source, CRHP can be a replacement to avoid superheating at the compressor outlet, and the heat sink can be upgraded as well [18]. In many application environments, when the temperature of heat sinks is over 100°C, the breakdown or degradation of the refrigerant is potential,

and increased wear and tear on the compressor components could decrease operational efficiency. For these problems, CRHP could be a solution with the wet compression technique employed. As a consequence, more details about the development of CRHP with respect to their working principles, isentropic compression performance, and associated wet compression concept need to be introduced in the next section.

1.2 Literature Review

In this chapter, the composition, working principles, and recent developments of CRHP are elaborated upon. The advantages of CRHP over VCHP in appropriate application scenarios are also worthy of description. The author particularly focuses on how the use of NH_3-H_2O as the refrigerant can improve the performance of CRHP, including the enhancement of the isentropic and volumetric efficiency of the compressor when wet compression is adopted. In addition, the technical improvement of compressors within CRHP has gradually become a hot spot. Many experimentally oriented or numerically oriented research studies have been conducted over the last twenty years with the aim of enhancing compressor performance. Therefore, collecting relevant technical research outcomes will assist the author in subsequent research.

1.2.1 Compression-Resorption Heat Pumps

To comprehend how the performance of various structures of VCHP and CRHP is measured and why, for industrial heating processes with large temperature glides, CRHP can achieve approximately 20% higher energy gain than that accomplished by VCHP, the concept of COP is explained [22]. Due to the conservation of energy, the heat removed from the heat source ($\dot{Q}_{source}$) together with the work done by the compressor ($\dot{W}_{comp}$) should equal the heat gained by the heat sink ($\dot{Q}_{sink}$), whose mathematical expression is defined as:

$$\dot{Q}_{source} + \dot{W}_{comp} = \dot{Q}_{sink} \tag{1.1}$$

To measure the efficiency of a heat pump in delivering heat to the heat sink per unit of work done by the compressor, COP is defined as follows:

$$COP = \frac{\dot{Q}_{sink}}{\dot{W}_{comp}} \tag{1.2}$$

Observed from these expressions, the COP of any type of heat pump is always greater than 1, meaning that environmentally friendly heat pumps can generate more high-quality heat than the work consumed by making the most of waste heat. The higher COP one type of heat pumps can achieve, the better its performance is. To achieve higher temperature values and larger temperature glides, a resorber and a desorber replace the function of the condenser and evaporator in CRHP, represented in Figure 1.2. Usually, mixture of the sorbent material and the refrigerant inside the resorber and desorber would take advantage of thermo-chemical sorption process to transfer heat [23].

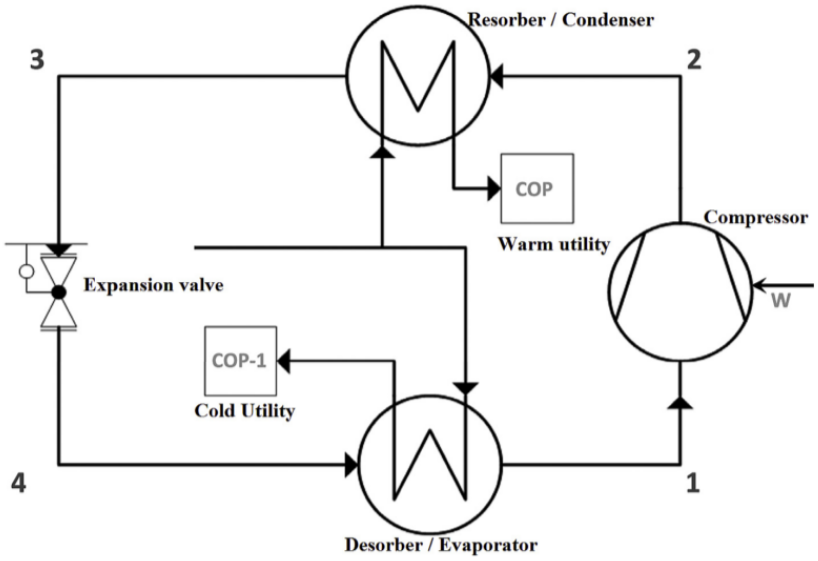

Figure 1.2: A schematic of a compression-resorption heat pump replaces the condenser and evaporator with a resorber and a desorber.

The key advantages of this process over vapor compression cycles lie in the ability of the sorbent material to store and release large quantities of energy gently in resorbers and desorbers, while dry vapor compression needs to experience significant temperature

differences that require plenty of work input. Take the NH_3-H_2O mixture as an example, the whole sorption process is listed as follows. In addition, typical temperature-enthalpy and temperature-entropy diagrams are shown in Figure 1.3 to help better understand these stages [15, 22].

- Desorption stage: heat is applied to trigger a chemical reaction that releases ammonia vapor from the low-temperature, low-pressure NH_3-H_2O mixture, and the desorption process is endothermic.
- Compression stage: the dilute ammonia solution enters the compression stage. A compressor raises the pressure and temperature of it, preparing well for the next stage.
- Absorption stage: the high-temperature, high-pressure dilute ammonia solution absorbs the ammonia vapor by releasing high-quality heat into the environment, and the absorption process is exothermic.

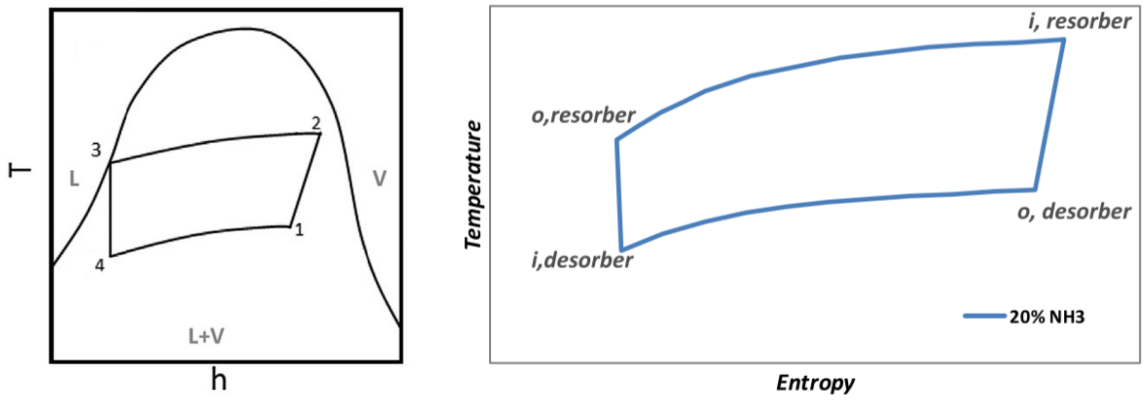

Figure 1.3: Temperature-enthalpy and temperature-entropy diagrams for CRHP when NH_3-H_2O mixture is used as the refrigerant. Data from van de Bor et al. (2014) and van de Bor et al. (2015).

Recently, V. Gudjonsdottir et al. investigated how the addition of CO_2 into an NH_3-H_2O mixture, as the refrigerant in CRHP, can improve the COP of the entire cycle under two different temperature glide settings [18]. From Figure 1.4(a), it is evident that with a temperature glide of only 40K, the addition of 5wt% of CO_2 generally

improves the COP by 18%, irrespective of the outlet vapor qualities. Conversely, as shown in Figure 1.4(b), when the temperature glide is 40K, the results are converse. Moreover, regardless of the outlet vapor qualities, the COP is consistently lower than in the previous case. Consequently, when considering the COP of refrigeration cycles, a ternary NH_3-H_2O-CO_2 refrigerant is beneficial only when the temperature glide is smaller than certain thresholds.

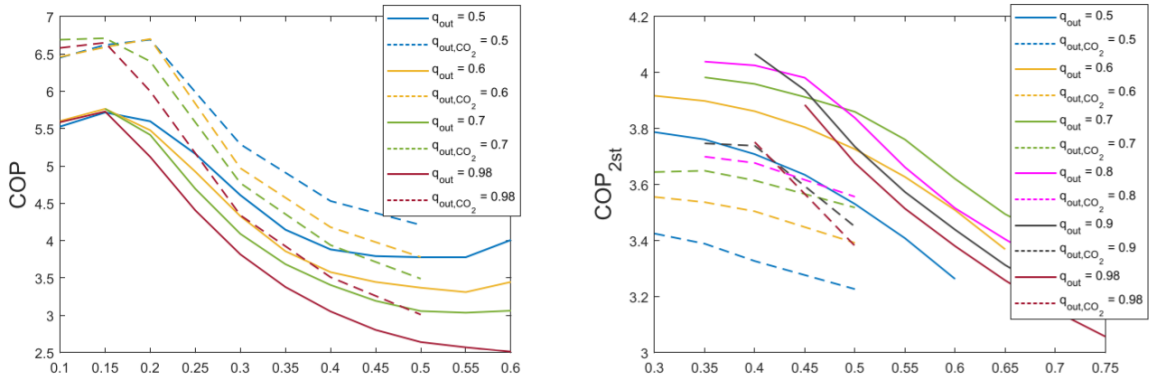

(a) the waste stream from 90 to 130 °C (b) the waste stream from 60 to 140 °C

Figure 1.4: COP as a function of ammonia concentration for various compressor outlet vapor qualities. The solid lines are the results for NH_3-H_2O and the dotted lines with extra 5wt% CO_2. Data from V. Gudjonsdottir et al. (2020).

Given that temperature glides can significantly impact the performance of CRHP, as discussed earlier, aligning the temperature glide of the heat sink and source with that of the working fluid during phase change becomes crucial for optimizing cycle performance. In a study by Benjamin Zühlsdorf et al., 14 different binary mixtures were explored as natural refrigerants to investigate the contribution of a well-matched glide to the increased performance of heat pumps [9]. The research revealed that setting the glides of the heat sink to 40°C resulted in cases with larger temperature glides in the heat source gaining more performance, as evidenced by an increase in COP of up to 20%. Furthermore, when situations leading to superheating at the outlet of compressors were avoided, the performance increase was even higher, reaching an upper limit of 27%. The result underscores the significant advantages of employing wet compression in CRHP systems. Therefore, the upcoming section will provide a comprehensive account of the

wet compression development employed in CRHP, comparing it with the conventional dry compression process in VCHP, given its frequent contemporary utilization.

1.2.2 Wet Compression Technique

In an ideal thermodynamic cycle system, neglecting energy losses, the work done by the compressor per unit time, the mass flow rate of the fluid passing through the compressor, and its enthalpy change can be expressed by the following relationship:

$$W = \dot{m} \cdot (h_2 - h_1) \tag{1.3}$$

In the isentropic compression process of an ideal gas, since the enthalpy change is positively related to the temperature change, reducing the temperature of the fluid medium inside the compressor can enhance the efficiency of the compressor, resulting in a higher COP for the overall cycle. In industrial production processes, various techniques can achieve this temperature reduction. Among them, inter-cooling of the fluid between stages, inter-fogging and wet compression are well-known methods. Zheng et al. investigated the topics of ideal and actual wet compression processes and demonstrated that inter-cooling could lead to a reduction in cycle efficiency [24]. Sepehr et al. studied the effects of evaporative cooling on gas turbine performance, incorporating both inlet fogging and wet compression in their investigation [25]. As is known, both inlet fogging and wet compression can lower the fluid temperature by injecting a fine mist of water droplets through nozzle sprays. What's more, the combined use of them can rise the power output to around 17% [26]. The enthalpy change of water, resulting from its evaporation, absorbs heat from the dry air. This leads to a denser fluid at the entrance and inside the compressor, allowing for an increased mass flow rate. They concluded that increasing the water injection in the inlet fogging system with saturated conditions at the compressor inlet air leads to a rise in the total compressor power consumption due to the increased mass flow rate. On the contrary, wet compression with increasing overspray can decrease the total compressor power consumption due to the effect of water droplet evaporation. Given the objective of enhancing the performance of the

cycle and preventing the occurrence of superheating, which is often observed at the exit of compressors in VCHP, it is essential to delve into the details of the wet compression development.

To understand how thermodynamic states of the air-water droplet mixture change during two-phase wet compression, Abhay et al. constructed a simple piston-cylinder system to simulate the entire process [27]. During this process, they recorded the pressure, temperature, and relative humidity accurately. Through the depiction of the P-V diagram, they found that compressing the mixture to a smaller volume can significantly save compression work, as shown in Figure 1.5.

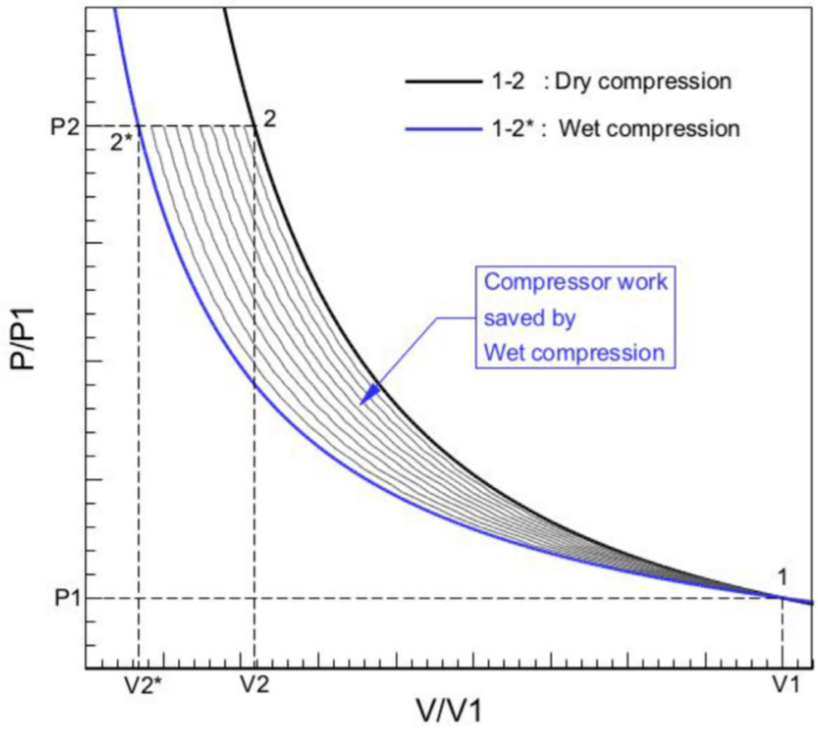

Figure 1.5: P-V diagram depicting both dry compression and wet compression processes. Data from Abhay Mohan et al. (2019).

They also conducted parametric studies based on the change in the starting relative humidity of the air, overspray percentage of water droplets, droplet diameter, and compression speed of the piston. They drew diagrams illustrating the deviation of P-V and T-V curves from dry air compression curves to observe how these variables affect the compression work demand.

Coincidentally, Hudson et al. conducted a thermo-fluid analysis on a simple flow model similar to the one utilized in the previous study [28]. The objective was to validate whether a higher percentage of overspray, smaller droplet diameters, and a slower compression rate could enhance the efficiency of the compression process. The outcomes from both experimental and simulation results are fundamentally consistent for the two research studies, and they underscore the significance of controlling variables such as overspray percentage and droplet diameter during wet compression.

By setting the water injection ratio and droplet average diameter to be 2% and 10 μm, Jianting et al. found that the pressure ratio and compression efficiency increased by 4.25% and 0.71%, respectively [29]. Through rigorous research by many scholars, it is highly reliable to conclude that wet compression helps improve the total pressure ratio and isothermal efficiency. Additionally, at the same total pressure ratio, this technique can decrease partial compression work.

While recent scientific research supports the idea that wet compression technology can reduce the temperature of the fluid inside the compressor, alleviating the load on the compressor and enhancing the performance of the thermodynamic cycle, some early research results clearly indicate that in many real-world application scenarios, when the conditions of isentropic compression are disrupted, the effectiveness of dry compression surpasses that of wet compression. Vorster et al. utilized 34 pure refrigerants and 31 zeotropic binary mixtures with varying compositions to evaluate how wet and dry compression affect heating COP when both re-entrant and bell-shaped T-S curves appear in the results [30]. The outcomes reveal significant inconsistencies compared to those discussed before. For all the analyzed refrigerants, those with re-entrant saturation vapor lines perform better when the refrigerants are superheated. Similarly, for refrigerants with bell-shaped T-S curves, only a few of them exhibit higher COP when wet compression is applied. Itard mentioned in the research that when irreversibilities in the cycle, such as non-isentropic compression, are considered, almost all the merits of wet compression will be lost [31]. This is apparently different from the case for an ideal fluid. As a consequence, in my research, for compressions involving two-phase

mixtures, the determination of whether wet compression is beneficial should depend on experimental and simulation results, especially when the non-isentropic compression condition is valid.

1.2.3 Overview of Twin Screw Compressor Research

Since the 1990s, a large number of studies on fluid flow inside screw compressors have emerged. Initially, due to the immature development of computer-aided software simulation technology, many scholars focused on using mathematical models and experimental methods to explore some challenging problems. These issues included the effect of pressure distribution on compressor performance, the complete thermodynamic processes inside compressors, and the phenomenon of leakage. The commencement of advanced experimental techniques, resulting from the accumulation of research in this field, holds significant guidance for current complex fluid research based on computational fluid dynamics (CFD).

Shizhong et al. conducted an experimental investigation to analyze the thermodynamic performance and characteristics, such as noise and pressure fluctuation, of twin-screw compressors [32]. They employed two methods, namely slide valve and variable-speed control, to regulate the refrigeration capability of these compressors. The results indicate that, when the volume flow rate reaches 381.07 $m^3 \cdot h^{-1}$, the use of variable-speed control yields superior noise reduction, enhanced COP, and overall efficiency compared to the other method [32]. The highlight of their experiment is the straightforward monitoring approach: six equidistant pressure sensors in the rotor chamber for both full-load and part-load conditions, coupled with a single-channel hand-held noise detection device measuring near-surface noise at 56 points, covering all suctions in the working chambers.

Usually, the working fluid in twin-screw compressors is a binary multiphase mixture with a variable gas void fraction (GVF). Different values of the GVF can affect the pressure distribution inside the working chambers of compressors. Feng et al. attached a small pressure transducer at the tail of the rotor to measure the pressure distributions

during the full rotation period [33]. Through building models of backflow and the working process by combining momentum equations and mass conservation equations in multiphase flow, and introducing variables such as discharge pressure, rotational speed, and inlet pressure, the research determined the optimal conditions of GVF, inlet/outlet pressure, and rotational speed for achieving a high-level pressure distribution.

Indicator diagrams serve as powerful tools for analyzing thermodynamic processes in twin-screw air compressors within the experimental field. To comprehend the impact of pressure ratio, rotating speed, and oil-to-gas ratio on the performance of oil-flooded compression, Xueyuan et al. integrated data from an embedded pressure sensor inside the female rotor to construct various indicator diagrams [34]. These diagrams documented obscure constant-volume compression due to gas back-flow resistance from the introduced oil, a sharp peak at the conclusion of the discharge process, and elevated pressure curves at larger oil-to-gas ratios. Through an analysis of the nature behind these phenomena, Xueyuan et al. draw the following conclusions:

- An oil-flooded screw compressor can operate at a large range of pressure ratios while achieving high efficiency due to the effect of over-compression, but this isn't favorable for energy efficiency.
- It is recommended to incorporate a flow-guiding slot near the discharge port to address the increased flow resistance.
- Constant isentropic efficiency is maintained over a large range of rotating speeds through a balance between increased compressor power consumption and enhanced volumetric efficiency.
- The suitable range for the oil-to-gas mass ratio is considered to be between 8:1 and 20:1 when accounting for associated cooling and lubricating effects.

In a nutshell, the performance of the working process of twin-screw compressors can be measured by considering factors such as pressure distribution, fluid leakage, and compressor parameters. Conducting experiments from various perspectives can assist

researchers in comprehending the impact of changes in key parameters on the final performance like GVF. Through the accumulation of numerous experimental try-outs, some intricate details like the unusual constant-volume compression have been figured out.

While various well-designed experiments on the performance of twin-screw compressors have uncovered the importance of key parameters and special phenomena, such as inlet/outlet pressure ratios and increased flow resistance near the discharge port, certain details like uneven pressure pulsations distributing along working chambers cannot be explained adequately without the use of CFD based simulation. The following paragraphs will elaborate on how the use of it helps explore additional details and identify defects in compression processes, ultimately contributing to further improvements in efficiency.

Among all the CFD simulations focusing on performance improvement, the study of non-uniform internal pressure distribution holds a prominent position. For instance, Bingqi et al. employed indicator diagrams to examine the formation of the flat section during compression and explore strategies for mitigating efficiency losses caused by uneven pressure distribution [35]. The pressure wave passing through the pressure sensor, caused by the rotor meshing, has been observed to create a spike followed by a drop. These phenomena form the fluctuation and flat sections in indicator diagrams, debating the cause of flat sections by leakage or resistance loss. Generally speaking, the lower the rotational speed, the weaker the pressure waves, and the fewer the flat sections, leading to a more uniform pressure distribution. To further reduce fluctuation and increase volumetric efficiency by about 3%, the end angle of the suction port can be delayed by around 18°, and a shorter radial suction port can be employed. This information was published in another article of their research [36], specifically when the rotating speed is about 3000 rpm. Similarly, Shizhong et al. also mentioned that the combination of the same suction delay angle and vapor injection port blocking can increase the volumetric and total efficiency by around 2% [37]. Additionally, when referring to the optimal delayed end angle, it is positively correlated with the rotational

speed, and the wrap angle can also affect efficiency by adjusting values of optimal suction delay.

During the investigation of various pressure characteristics of compressors, the features of stagnant pressure rise and suction/discharge port pressure losses are worthy of in-depth analysis. Shizhong et al. also employed indicator diagrams in an attempt to fully understand how suction pressure loss near the suction end (SESPL) and stagnant pressure rise in the compression process (CPSPR) were caused [37], as is shown in Figure 1.6. This analysis is crucial due to their practical significance in understanding unpredictable efficiency losses.

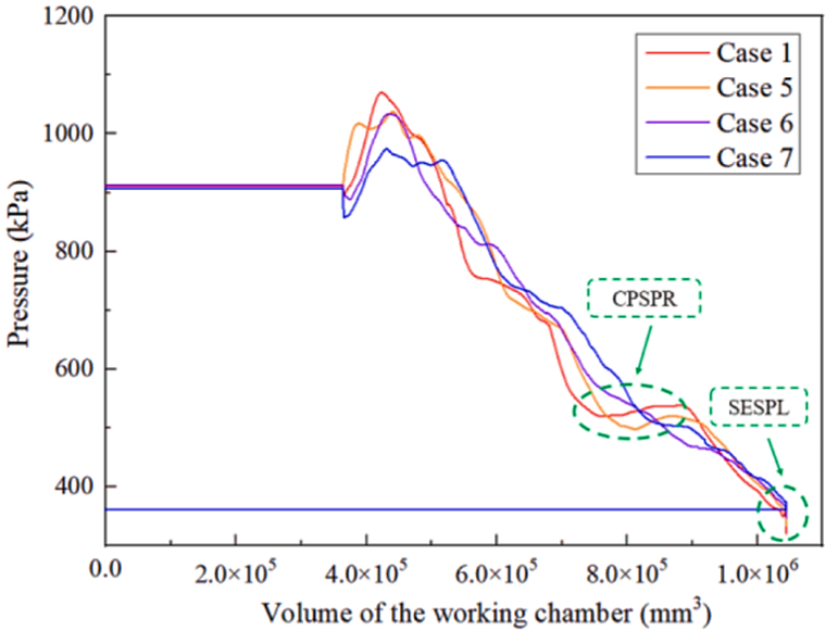

Figure 1.6: Phenomena of SESPL and CPSPR occurring in the P-V diagram of the compression process. Data from Shizhong et al. (2021).

The occurrence of SESPL is usually attributed to flow obstruction in the radial suction part of the male rotor, as the flow area of the male rotor is consistently smaller than that of the female rotor before the suction chamber disengages from the working chamber. Additionally, a higher evaporation temperature can amplify SESPL and cause the phenomenon to start earlier due to increased gas density and more severe flow obstruction. To alleviate this situation, different delay angles for axial and radial

suction ports should be set. The delay angle for the male rotor's radial suction should be larger to compensate for the negative effects of the larger flow area on the female side. The delay angle for the axial suction port can be the same for both male and female rotors since their change process is synchronous.

Apart from this, the presence of the closed cavity in the vapor injection port can result in CPSPR, thereby increasing the burden on the indicated power of the compressor and reducing overall efficiency. However, under varying condensing temperatures, which can influence the extent of the SESPL phenomenon, the pressure loss of CRSPR undergoes slight changes. Consequently, when vapor injection is not carried out, only the action of blocking and reducing the volume of the closed cavity is necessary to prevent the occurrence of the CPSPR phenomenon.

In addition to examining the impact of pressure distribution on compressor efficiency, there is a significant need for extensive research into pressure pulsation. This is particularly crucial due to its potential to inflict damage on internal components of compressors. Under conditions of high oil flow rate, the abrupt increase in pressure pulsation at the axial oil injection port may lead to fluid hammer. To mitigate the adverse effects of fluid hammer, researchers have explored the construction of an orifice along the oil path, as suggested by Yang et al. [38]. In the context of simulation studies concerning pressure distribution, pressure pulsation, and efficiency improvement, the mesh generation of the CFD model stands out as a crucial step that significantly influences the subsequent performance quality. Specifically, notable researchers in the field, affiliated with the Centre for Positive Displacement Compressor Technology at City University London, have conducted extensive studies on grid generation strategies. Therefore, it is crucial to delve into a discussion of their analyses and breakthroughs in it.

Approximately a decade ago, Kovacevic et al. initiated the development of a sophisticated, custom algebraic grid generation algorithm tailored for application in twin-screw compressors featuring both variable and uniform pitch rotors [39, 40]. This grid optimization enables an elevated internal pressure buildup and enhanced volumetric efficiency for rotors with varying leads. The outcome is attributed to an enlarged

discharge port area, consequently leading to diminished throttling losses and sealing line length in comparison to the uniform pitch configuration. Due to an immature customized grid generation algorithm for screw compressor topologies like tri-screw rotors, Rane et al. introduced key-frame re-meshing [41]. The main focus is irregularly supplying pre-generated unstructured meshes to the CFD solver. In a simulation of a reversible adiabatic compression process, three generation methods were tested: diffusion equation mesh smoothing, user-defined nodal displacement, and key-frame re-meshing. Unfortunately, the last method resulted in accumulating errors in state predictions over successive compression cycles, with poor accuracy and time efficiency. Researchers unanimously agree that only customized tools for grid generation are worth in-depth analysis, guiding subsequent research.

For the sake of simplification, other classical screw compressor fluid research branches that are not strongly related but have profound core are summarized, whose hightlights are shown in Table 1.1.

Table 1.1: Summary of some classical screw compressor fluid research branches.

Reference	**Highlights**
Sham Rane et al. (2020).[42]	Using SRK and ARK equations instead of the ideal gas equation yields closer performance in expander simulation results.
A. Kovacevic et al. (2010).[43]	Expanding the scope of CFD applications can be achieved by incorporating turbulence models beyond the existing $k-\epsilon$ model.
Huagen Wu et al. (2020).[44]	Identifying the optimal vapor injection pressure and position allows pinpointing the highest compressor efficiency.

1.3 Individual Research Objective

By sorting out the work of previous researchers on improving CRHP performance, the objective of this research is stated as follows:

Simulating wet compression processes in CRHP cycles using Ansys CFX to enhance cycle volumetric efficiency and COP, considering compressible, turbulent, and multiphase features of NH_3-H_2O mixture as the working fluid.

To study compressible, multiphase, turbulent flow in a twin-screw compressor, we will create a 3D geometric model. High-quality hexahedral movable meshes will be generated using SCORG and Twinmesh, and compared for mesh independence. The static parts will be meshed with Fluent Meshing. Compressible, turbulent airflow will be introduced using real gas equations, like the PR equation, for validation. Initial validation with a single inlet and outlet will be compared to previous experiments. An NH_3-H_2O mixture will then analyze pressure distribution, pulsation, and the effects of return flow and composition changes. Based on simulation results, strategies to improve COP and overall efficiency in CRHP will be proposed.

In order to perform these tasks clearly, the following steps are elaborated upon as detailedly as possible:

- The oil-free compressor will be modeled in Fusion 360, incorporating lobe combination, built-in volume index, and shaft speed. Initially, the return flow pipeline will be excluded, focusing on a single inlet and outlet.

- Rotor grid meshing will utilize Twinmesh to form a control group for comparison. The static housing structure will be meshed with Ansys Meshing for simplification. Finally, mesh quality independence analyses will be conducted.

- Model validation of the single-phase, compressible, and turbulent airflow will be performed using Ansys CFX as the solver and CFX-Post for post-processing. Simulated and experimental results for the pressure coefficient and velocity distribution along the compression chamber path will be graphed together to assess modeling accuracy.

- The complex mathematical model for advanced simulation analyses of the non-equilibrium NH_3-H_2O mixture in the compression process needs to be deduced first. The study incorporates theories of compressible fluid dynamics, kinetic turbulence energy, multiphase flow.

- In the final and most complex CFX model, the return flow pipeline is added as a significant feature. The simulation will incorporate all the developed mathematical models and insights from previous research, including seal mass fraction and back flow balance. The simulated results will be compared with experimental data from a related project.

- Organize simulation data and its comparison with experimental one, complete thesis writing and prepare for the final defense.

Finally, the timetable for the concise statement and arrangement of all procedures depicted above is presented in Table 1.2.

Table 1.2: The timeline research for the author's project, months are shorted to the first character.

Task	**N**	**D**	**J**	**F**	**M**	**A**	**M**	**J**	**J**
Literature review									
Geometric modelling of the compressor excluding the return flow pipeline									
Meshing of rotors and static housing along with their independence verification									
Single-phase, compressible and turbulent airflow simulation using Ansys Fluent and Tecplot 360 for reliability analysis									
Mathematical modelling of the non-equilibrium multiphase mixture considering both fluid dynamics and thermodynamics									
Simulation of the ammonia-water mixture including the return flow pipeline, together with the performance assessment									
Thesis writing and preparation for final defense									

Chapter 2

Geometric Modelling and Meshing

2.1 Simplification of the Geometric Model

Initially, the 3D modeling of the oil-free twin-screw compressor needs to be conducted based on the existing industrially used compressor housed in the laboratory for subsequent CFD simulation and analysis. However, duplicating the entire structure of the real compressor perfectly in the software isn't prudent since certain auxiliary parts such as bearings, washers, and threaded holes are irrelevant to the complex flow simulation. Moreover, supportive structures like the base, sealing cover, and irregular shapes that won't affect the flow characteristics need to be simplified. The most significant features, including rotor profiles, screw features, and shapes of the suction and discharge chambers, must be captured as detailedly as possible. Given that detailed parameters of twin screw meshing rotors of the real compressor are lacking due to trade secret protection, all non-directly measurable parameters necessary for modeling are obtained from reasonable assumptions, relevant literature searches, and other parameter correlation expressions. In general, this research divides the whole fluid modeling into three domains: the suction domain, the discharge domain, and the screw domain. The first two fluid domains are inside the suction and discharge chambers of the stator, while the screw domain are areas between the male and female rotors and between the rotor and the stator of the compressor. The assembly of the model and the real compressor are

shown in Figure 2.1. In addition, both chambers and rotors of the model are depicted in Figure 2.2. Furthermore, in order to express the relationship between the various components of the compressor accurately and normatively, its fluid domains and solid domains are described in Figure 2.3.

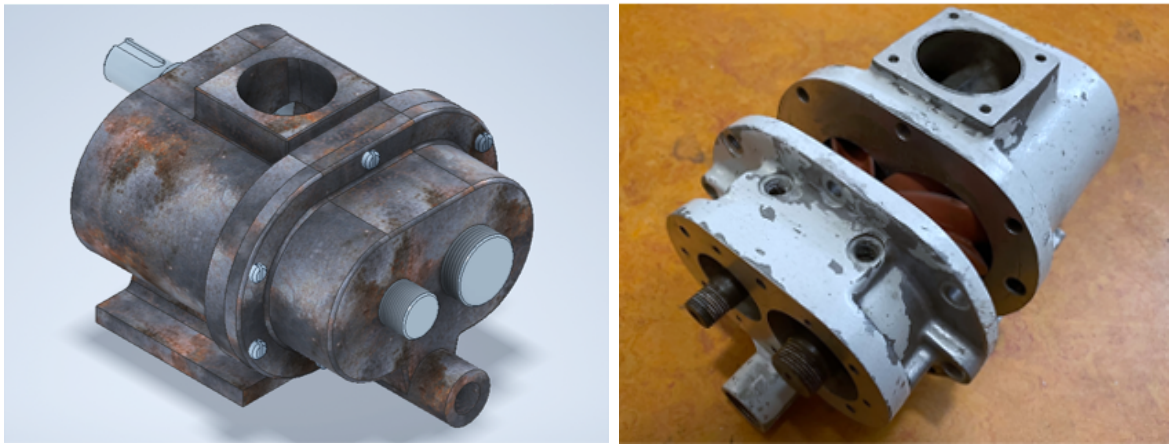

(a) the assembly of the 3D model (b) the profile of the real compressor

Figure 2.1: Profiles of the assembly and the real compressor.

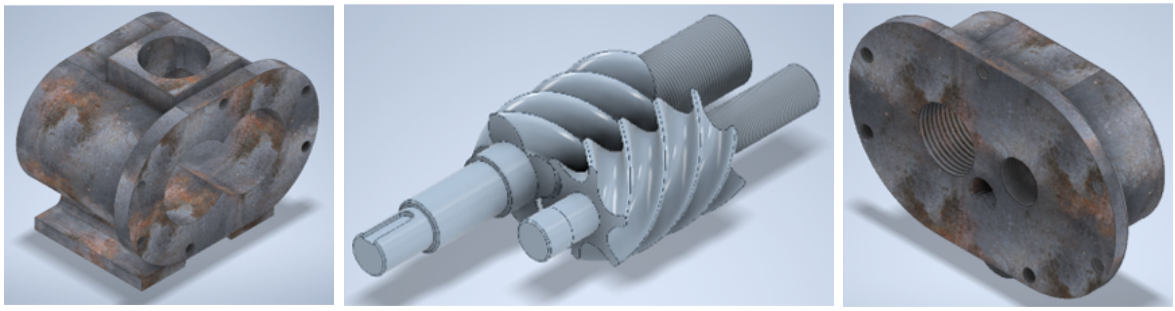

(a) the suction chamber (b) the meshing rotors (c) the discharge chamber

Figure 2.2: Appearances of all the components of the modelled screw compressor.

The oil-free compressor in this study features an SRM "D" rotor profile with a 4/6 lobe combination. The configuration and dimensions of the compressor are detailed in Table 2.1. Specifically, the rotor tip and inter-lobe clearances are minimized compared to the designed values to enhance the sealing and pressurization effects of the fluid. The reliability of this adjustment has been verified by several previous research studies [37, 42]. However, a tiny gap is still maintained to prevent negative volume and excessive

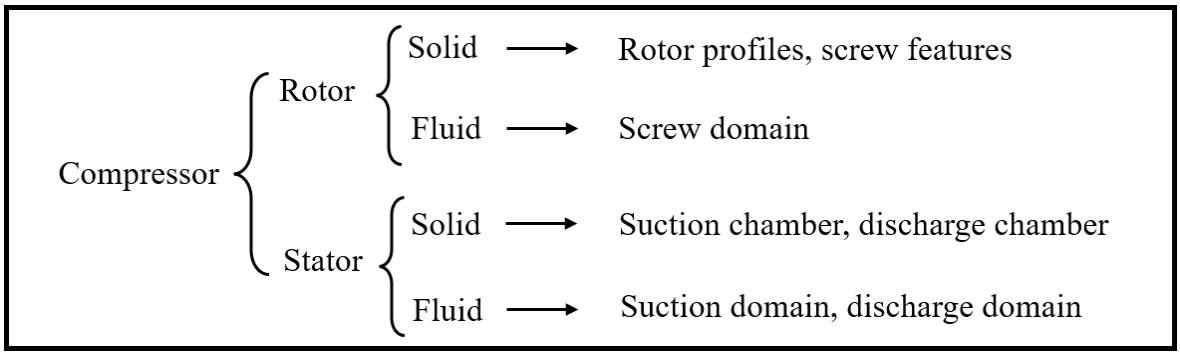

Figure 2.3: The classification of different solid and fluid domains of the compressor.

pressure inside the enclosed cavity [35]. Furthermore, the end clearances in suction and discharge domains are neglected in this study. This decision is based on the omission of heat loss due to friction between the stator and meshing rotors, and the occurrence of external leakage is considered negligible as well. In addition, the animation depicting the high-speed rotation of the rotors and their profile meshing using the generating method has been created in CAXA.

Table 2.1: Screw compressor geometric characteristics.

Parameter	**Value**
Rotor profile	SRM "D" profile
Rotor lobe combination	4/6
Rotor centre-distance [mm]	51
Male rotor outer diameter [mm]	65.5
Female rotor outer diameter [mm]	64.5
Rotor length [mm]	86
Male rotor wrap angle [degrees]	300
Rotor tip clearance [mm]	0.015(0.080)
Inter-lobe clearance [mm]	0.030(0.030)
Suction end clearance [mm]	0(0.200)
Discharge end clearance [mm]	0(0.050)

2.2 Meshing for the Fluid Domains

The complexity of meshing primarily lies in the intricate structural design and operational characteristics of the highly rotational twin-screw compressor. As mentioned in the previous section, achieving suitable pressurization and ensuring sealing capacity necessitates extremely small inter-lobe and rotor tip clearances. This requirement poses a significant challenge for grid meshing in the screw domain, as a substantial amount of ultra-precise boundary layer meshes is needed. Furthermore, during the high-speed rotation of rotors, the internal control volume at the edge of the screw domain undergoes continuous and intensive changes, leading to grid deformation and further complicating the meshing process.

To ensure an accurate representation of grid deformation and flow characteristics, a combination of structured and unstructured grids is employed. Structured grids, renowned for their regularity and numerical stability, are ideal for meshing central sections of the suction chamber and discharge chamber, as well as that of rotors, using hexahedral-based grids. Otherwise, high-quality unstructured meshes for the screw domain are generated using TwinMesh from CFX Berlin. The rotor tips, with exceptionally high aspect ratio (φ), require flexible grid meshing. Additionally, unstructured grids facilitate local refinement at boundary layers of the screw domain. This blend of structured and unstructured grids supports high-quality grid generation across the entire compressor.

2.2.1 Stator Meshing in Fluent Meshing

At first, the stator meshing was generated in Fluent Meshing, considering the convenience and compatibility of data connection with Ansys Fluent during the solving procedure. The suction chamber and discharge chamber were regarded as two independent geometries, with their interface grid consistency requirement needing to be fulfilled by applying the share topology technique (STT) in Fluent Meshing, as illustrated in Figure 2.4(a). To ensure smooth transition of the structured grid from one orange surface of the partial enlargement to the other, satisfying the continuity equa-

tion in the solver, surface joining was attempted three times in areas where the gap distance between the two surfaces is smaller than 0.4 mm. More detailed settings of STT are depicted in Figure 2.4(b). After applying the SST and generating the surface mesh, a smooth-transition boundary layer was added in fluid domains, growing on the solid-fluid interface to ensure accurate capture of viscous sublayers of turbulent flow near walls. Finally, the poly-hexcore method was adopted to generate a mixed structured and unstructured volume mesh, whose section view was represented in Figure 2.5. Further details on the quality of the stator meshing are outlined in Table 2.2.

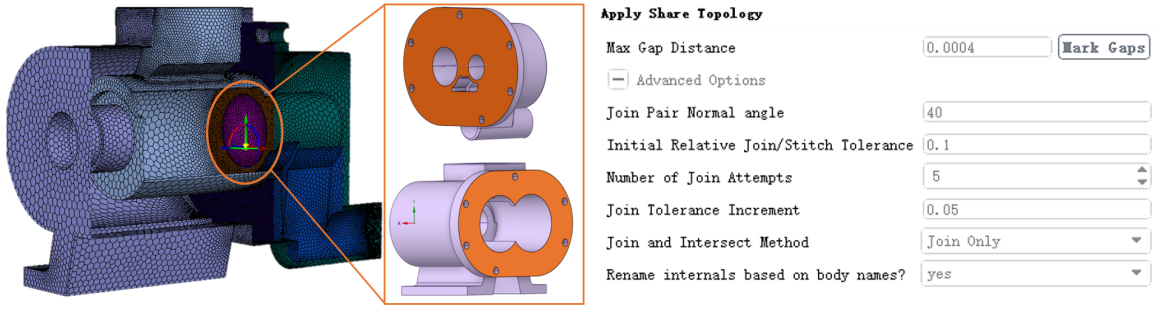

(a) the schematic diagram of STT (b) parameter settings of STT

Figure 2.4: The schematic diagram and detailed parameter settings of STT applied to interfaces of suction and discharge chambers.

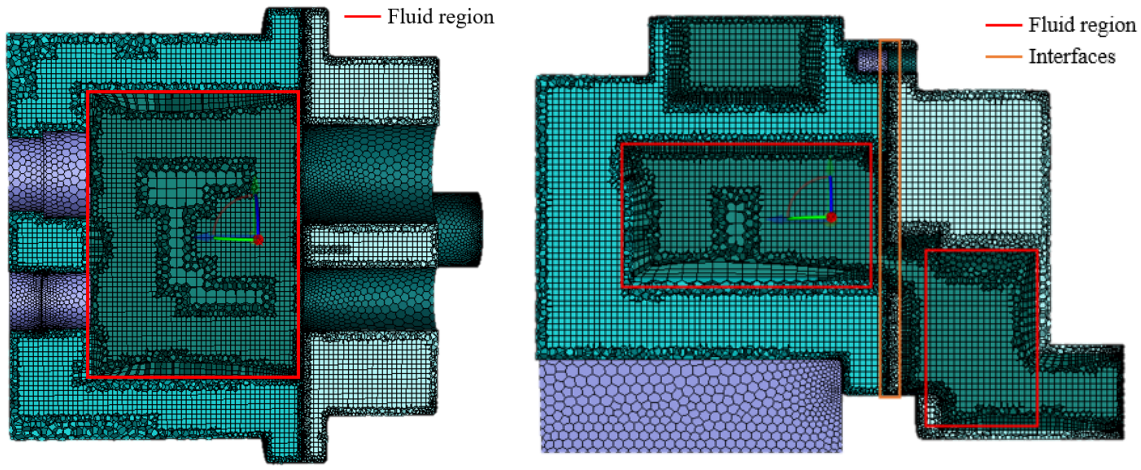

(a) top view of the volume mesh (b) front view of the volume mesh

Figure 2.5: The top and front section views of the stator volume mesh with fluid domains and interfaces marked.

Table 2.2: Quality assessment of the stator grid generated in Fluent Meshing.

Parameter	**Value**
Cell count	603158
Minimum orthogonal quality	0.19
Average orthogonal quality	0.95
Maximum aspect ratio	49.31
Average aspect ratio	2.14
Maximum skewness	0.81
Average skewness	0.05

2.2.2 Stator Meshing in Ansys Meshing

After observing that many researchers studying twin-screw compressors only generate grids for fluid domains, and summarizing from recent studies that the combination of Ansys CFX and TwinMesh for analyzing highly rotational compressible flow phenomena is more stable than using Ansys Fluent, but doesn't accept the grid from Fluent Meshing, it's worth exploring the generation of fluid domains for the stator again in Ansys Meshing and then comparing the results with those from Fluent Meshing [38, 45]. The original shape of the discharge domain is too irregular to ensure flow uniformity. Additionally, a large amount of unstructured grid is adopted at its edges, increasing aspect ratio and decreasing orthogonal quality. While the original shape closely approximates the real dimensions, it has the potential to hinder convergence, which should be avoided. To address these issues, necessary revisions have been made, facilitating smoother fluid transport from the screw domain to the discharge domain and reducing the occurrence of irregular edges, all while ensuring adherence to the symmetry principle. Meshed fluid domains of both original and revised stators adopting hex dominant method are demonstrated in Figure 2.6, with the number of nodes and elements included.

After completing the stator meshing for all three different geometries, a basic summary of their qualities judged from different perspectives is presented in Table 2.3. Only averages are used to reflect their performance as objectively as possible. It's observed

that the number of elements generated in Fluent Meshing is at least twice as much as those from Ansys Meshing. However, its grid quality, based on selected averages, is much better. This reflects the performance advantages of the officially built workflow: it sets all possible working conditions for users in advance, and users only need to make the optimal choice to generate a grid that fully meets the requirements.

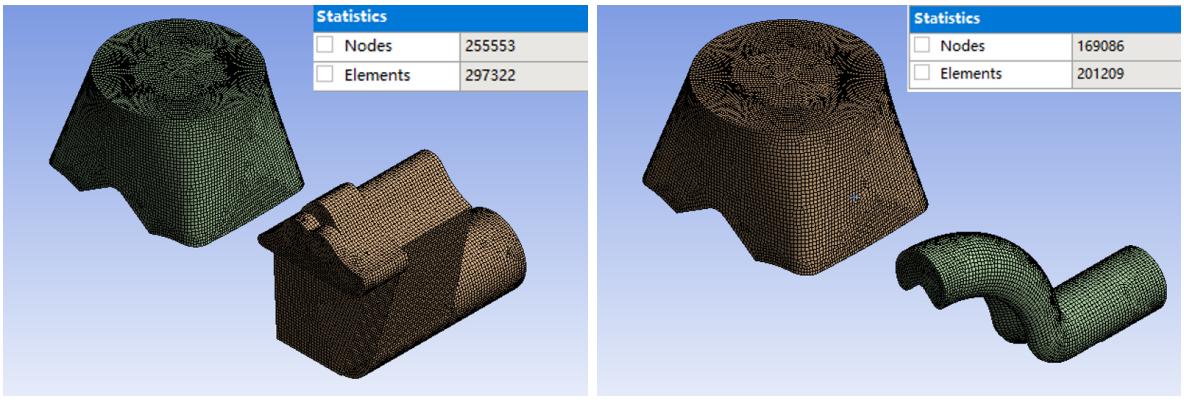

(a) volume mesh: original geometries (b) volume mesh: revised geometries

Figure 2.6: The appearance of volume meshes for the original and revised geometries, along with the corresponding nodes and elements data, in Ansys Meshing.

Table 2.3: A summary of qualities of meshing generated in Fluent Meshing and Ansys Meshing separately. #1: original stator in Fluent Meshing, #2: original stator in Ansys Meshing, #3: revised stator in Ansys Meshing.

Parameter	**Value(#1)**	**Value(#2)**	**Value(#3)**
Cell count	603158	297322	201209
Average orthogonal quality	0.95	0.77	0.75
Average aspect ratio	2.14	3.36	3.06
Average skewness	0.05	0.33	0.37

2.2.3 Rotor Meshing in TwinMesh

The simulation aims to calculate fluid flow and pressure distribution within this oil-free screw compressor. Prior to conducting the transient three-dimensional CFD simulation in Ansys CFX, deforming meshes of the screw domain around the rotors are generated

using TwinMesh. It adopts a mixed meshing method wherein nodes are fixed on the female rotor and can move along all other curves, ensuring an accurate representation of the complex female rotor geometry. During movement, the nodes along the interface curve can fit together, further enhancing mesh accuracy. Additionally, the axial gap flow will be considered by utilizing additional gap meshes created by TwinMesh, which are further divided into axial gap MZ and axial gap PZ, representing gap meshes on the front and back rotor faces, respectively. Consequently, the whole fluid domain for rotor meshing in TwinMesh can be manually divided into three sub-regions: screw domain meshing, axial gap MZ meshing, and axial gap PZ meshing, and more detailed procedures are outlined in Figure 2.7.

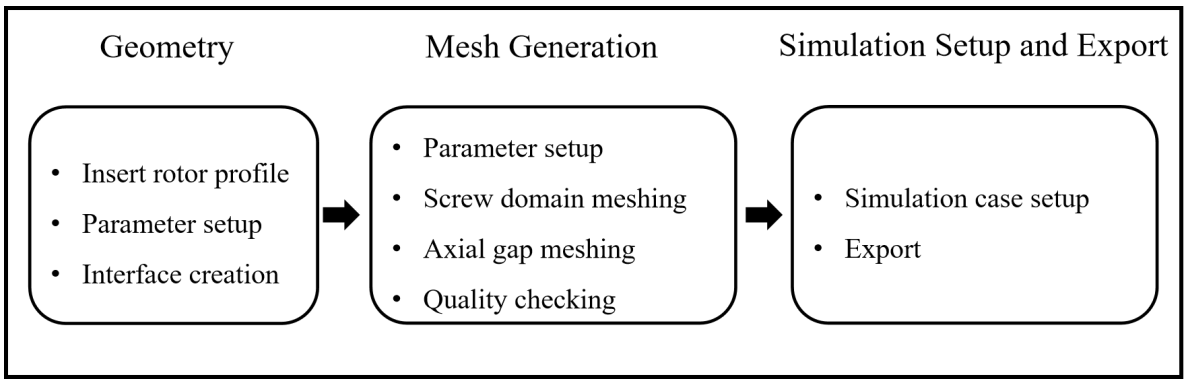

Figure 2.7: The schematic diagram illustrating main procedures followed to generate deformable rotor meshing in Twinmesh.

Initially, 2D planar rotor profiles are imported. TwinMesh then draws casing lines based on specified rotor diameters. Additionally, TwinMesh determines the interface zone, which constrains the area for automatic interface generation between both rotor fluid meshes of the screw domain. A detailed presentation of the geometry drawing is provided in Figure 2.8. Given that the wrap angle for this screw compressor is 300 degrees and the pitch angle is 90 degrees by default, 390 sections of meshes will be generated for one full rotation, ensuring that details of mesh deformation in each angle can be accurately captured. Once all parameters are suitably adjusted, interfaces in 390 mesh sections are generated successfully.

TwinMesh adopts a two-step meshing strategy for all mentioned sub-regions to

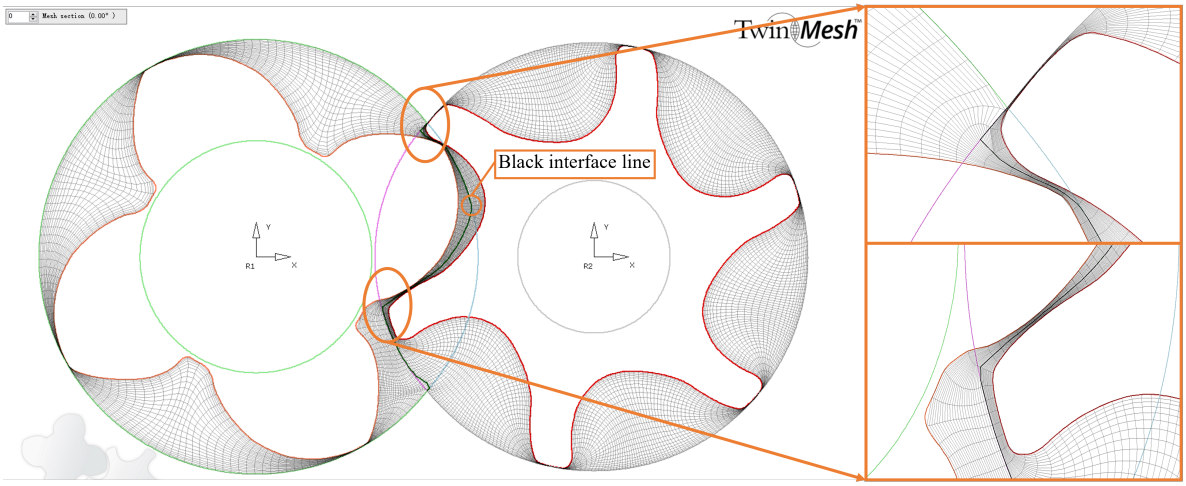

Figure 2.8: The schematic diagram presenting the generation of the interface at the starting position of the rotation with local enlargements included.

ensure both efficiency and quality of the meshing result. The initial meshing at 0 degrees is crucial, as subsequent meshes are based on the first one when using the "mixed" meshing type. The pre-smoothing iterations for the initial mesh are set at 8000, and it decreases to 500 for subsequent meshing. The number of radial divisions and circumferential nodes are the two most prominent variables that affect the quality of the initial and subsequent meshing. A higher number usually leads to more refined control volume features, resulting in a larger min angle (ϑ) (minimum orthogonal angle for mesh quality) and smaller φ, which prepares well for the following CFX simulation. In the user guide, ϑ in each 2D section is recommended to be over 18 degrees, and each φ should be smaller than 1000, which has been fully satisfied except for Mesh05. The reason behind it is the coarse circumferential grid for Mesh05. Specifically, circumferential nodes are set for the female rotor to achieve a 1:1 circumferential node ratio for the rotors. Additionally, the number of axial sections will control the size of elements longitudinally in each one of the 390 meshing sections.

Among all parameters to be set, in general, the combination of maximum element size, radial divisions, circumferential nodes, and axial sections determines well the tendency of meshing quality and element number. Default values from TwinMesh and some recommended combinations from recent studies would result in an oversized ele-

ment number, requiring much more computational resources than the setting from Rane et al [42]. After the screw domain meshing is completed, the same steps are followed in 2D axial gap PZ and MZ, respectively, whose quality assessment is also based on ϑ and φ. Quality assessments of structured 2D meshing in all three sub-regions are represented in Figure 2.9 and Figure 2.10, while that of 3D meshing is shown in Figure 2.11. In this study, eight sets of rotor meshing cases are compared to complete the mesh independence study, with the radial, axial and angular divisions kept the same as 7, 136 and 1 degree. This is because changes in these three variables do not significantly affect mesh quality or simulation results [42]. The main variables and meshing quality are demonstrated in Table 2.4. Among them, Mesh01 is taken as the reference, with three-dimensional divisions the same as those used by Rane et al. [42]. From Mesh01 to Mesh05, all variables except for the circumferential nodes are fixed to observe how the number of nodes influences the simulation result. From Mesh06 to Mesh08, the only variable changed is the maximum element size, to determine at what point an increase in size deteriorates the simulation results.

Moreover, TwinMesh automatically configures the simulation case for Ansys CFX-Pre upon completing the meshing process. Notably, it uniquely incorporates the non-reflecting boundary condition in the setup, facilitating the passage of pressure and density waves through the boundary with minimal reflection, particularly in compressible flow scenarios. Finally, the rotor and stator meshing are combined to be exported into CFX-Pre for the following mesh independence study and performance analysis of the single-phase ideal airflow simulation.

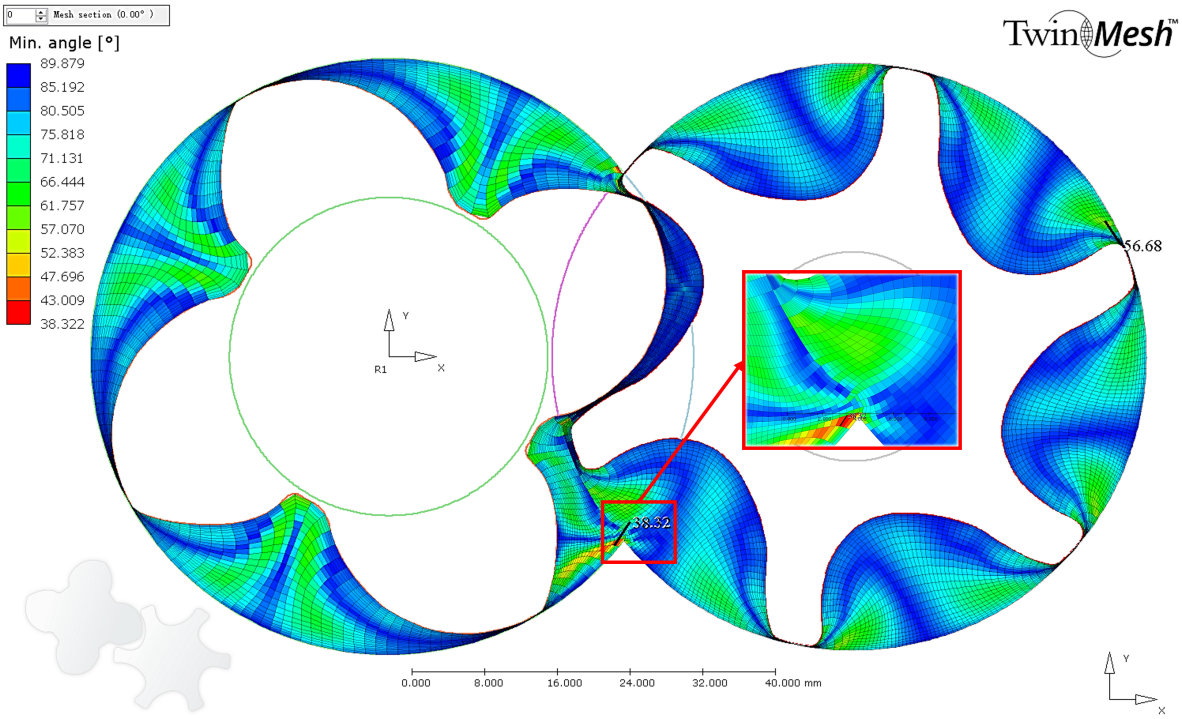

Figure 2.9: Quality assessment: min angle of structured 2D meshing of the screw domain.

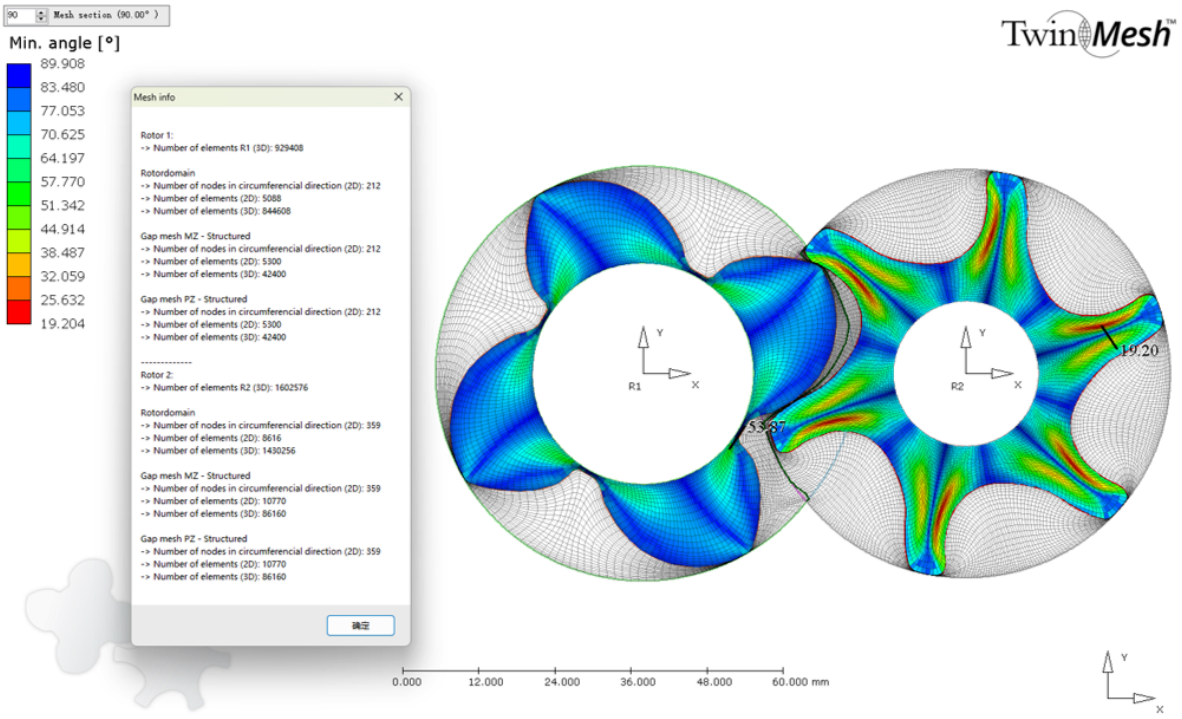

Figure 2.10: Quality assessment: min angle of structured 2D meshing of the axial gap PZ and MZ. Their number of elements and shapes are the same.

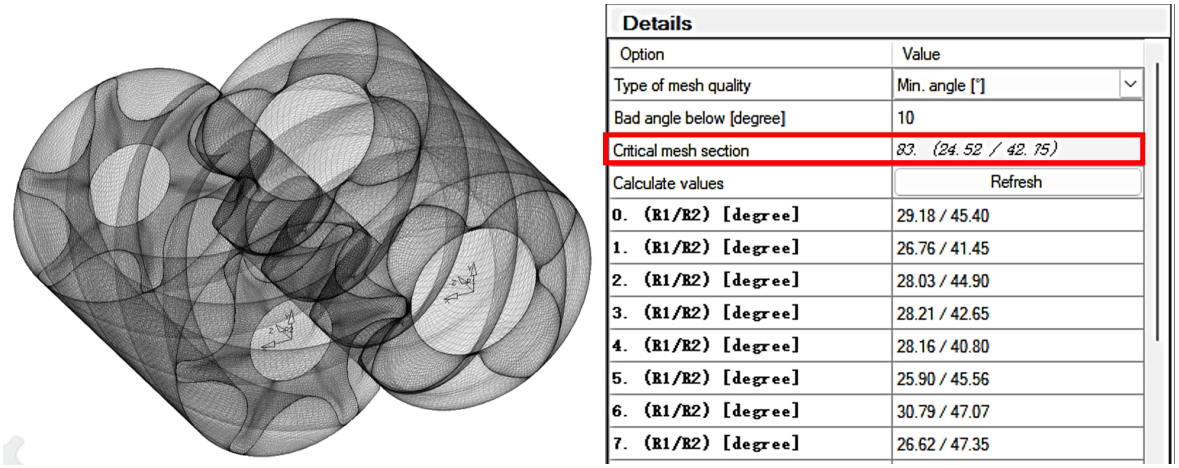

(a) structured 3D meshing

Details

Option	Value
Type of mesh quality	Min. angle [°]
Bad angle below [degree]	10
Critical mesh section	83. (24.52 / 42.75)
Calculate values	Refresh
0. (R1/R2) [degree]	29.18 / 45.40
1. (R1/R2) [degree]	26.76 / 41.45
2. (R1/R2) [degree]	28.03 / 44.90
3. (R1/R2) [degree]	28.21 / 42.65
4. (R1/R2) [degree]	28.16 / 40.80
5. (R1/R2) [degree]	25.90 / 45.56
6. (R1/R2) [degree]	30.79 / 47.07
7. (R1/R2) [degree]	26.62 / 47.35

(b) min angle for 390 axial sections

Figure 2.11: Quality assessment: structured 3D meshing view and a list of min angle for 390 sections including the smallest one.

Table 2.4: Main variables and minimum min angle of eight sets of rotor meshing cases selected.

Case	ϑ [°]	**Maximum size [mm]**	**Circumferential node**	**Element**
Mesh01	29.18	1	200	737,153
Mesh02	26.26	1	360	945,793
Mesh03	26.26	1	160	684,993
Mesh04	28.60	1	240	789,313
Mesh05	17.05	1	120	632,833
Mesh06	28.71	1.2	200	690,209
Mesh07	22.17	1.4	200	658,913
Mesh08	22.17	2.0	200	596,321

Chapter 3

CFX Simulation for the Ideal Single-phase Airflow

The selection of air as the ideal gas for the single-phase turbulent simulation represents the simplest material features and simulation outcomes while retaining the main characteristics of high-speed compressible flow inside the twin-screw compressor, making it a good choice for validating the reliability and practicability of the model, conducting mesh independence studies, and preparing for the next, more sophisticated multi-phase flow simulation. Initially, initial and boundary conditions, total energy heat transfer models, turbulent models, and other main parameters are well considered in CFX-Pre, where user-defined expressions are added to monitor the dynamic simulation process. In CFX-Solver, convergence is primarily judged from three aspects: residual analysis, variable imbalances, and monitoring of user-defined expressions. Finally, the distribution of main parameters such as global pressure and temperature is further analyzed via CFX-Post, contributing to mesh independence studies and understanding their influence on the performance of flow inside compressors.

In addition, the governing equations and global parameter settings need to be briefly explained to prove the theoretical feasibility of the simulation. Specifically, heat transfer between fluid domains and surfaces of rotors and stators is well considered in the total energy equation, which reflects the real situation well.

3.1 Governing Equations and Simulation Settings

3.1.1 Govern Equations

Governing equations controlling the dynamic development of the flow are not as complicated as those in multi-phase flow. They mainly include the conservation laws of mass, momentum, total energy, and geometry. Specifically, a geometric conservation equation is fully considered in this study, given that the grid velocity $\boldsymbol{U_g}$ and the grid motion do not depend on the fluid motion [41]. The complete form of mass conservation of the ideal airflow is equivalent to the continuity equation in differential form considering the compressibility, as shown in Eq. 3.1:

$$\frac{\partial \rho}{\partial t} + \nabla \cdot (\rho \boldsymbol{U}) = 0 \tag{3.1}$$

where ρ is the density of the airflow, $\boldsymbol{U}$ is the velocity vector; t is the computational time. Further, the momentum equations considering external forces are also written in the complete form with the compressibility factor included, as shown in Eq. 3.2:

$$\frac{\partial (\rho \boldsymbol{U})}{\partial t} + \nabla \cdot (\rho \boldsymbol{U} \otimes \boldsymbol{U} + p\boldsymbol{I}) = \rho \boldsymbol{F} \tag{3.2}$$

where p is the pressure of the airflow, $\boldsymbol{I}$ is the second order unit tensor, and $\boldsymbol{F}$ is the external force exerted by unit mass of the airflow. In addition, the total energy equation, rather than the thermal energy equation, is adopted, given that high-speed flow with a Mach number (Ma) exceeding 0.2 and pressure wave capture are important features in this simulation. The viscous work term is also considered. And the expression is shown in Eq. 3.3:

$$\rho \frac{D}{Dt}\left(\breve{u} + \frac{\boldsymbol{U} \cdot \boldsymbol{U}}{2}\right) = \rho \boldsymbol{U} \cdot \boldsymbol{f} + \nabla \cdot (\tau_{ij} \boldsymbol{U}) + \nabla(\lambda \nabla T) + \rho \dot{q} \tag{3.3}$$

where $\breve{u}$ is the internal energy of the airflow, $\boldsymbol{f}$ is the body force of the airflow, τ_{ij} is the surface shear stress tensor, λ is the thermal conductivity, T is the temperature of the airflow and $\dot{q}$ is the unit thermal radiation received by the airflow. Furthermore,

geometric conservation is enforced to ensure the complete preservation of the aforementioned equations, which can be regarded as mass conservation under the condition that $\boldsymbol{U} = 0$. This is accomplished by accounting for the motion of cell faces and explicitly calculating the grid velocities [41]. The corresponding expression is presented in Eq. 3.4:

$$\frac{d}{dt}\int_{\Omega} d\Omega - \int_{S} \boldsymbol{U_g} \cdot \boldsymbol{n} dS = 0 \tag{3.4}$$

where Ω is the control volume changing with time and S is the control surface. Given the turbulent nature of compressible airflow within the high-speed rotation of the twin-screw compressor, the entire fluid domain must adhere to an additional turbulent transport equation. In this simulation, the shear stress transport (SST) model is employed, taking into account both intricate fluid flow phenomena and constrained computational resources. Consequently, the merits of the $k-\omega$ model for near-wall region calculations and the advantages of the $k-\epsilon$ model for far-field calculations are both leveraged [37]. The expressions for these models are presented in Eq. 3.5:

$$\begin{aligned}
\frac{\partial(\rho k)}{\partial t} + \frac{\partial}{\partial x_j}(\rho U_j k) &= \frac{\partial}{\partial x_j}\Big[(\mu + \frac{\mu_t}{\sigma_k})\frac{\partial k}{\partial x_j}\Big] + P_k - \tilde{\beta}\rho k\omega \\
\frac{\partial(\rho \omega)}{\partial t} + \frac{\partial}{\partial x_j}(\rho U_j \omega) &= \frac{\partial}{\partial x_j}\Big[(\mu + \frac{\mu_t}{\sigma_\omega})\frac{\partial \omega}{\partial x_j}\Big] + \alpha\frac{\omega}{k}P_k - \beta\rho\omega^2
\end{aligned} \tag{3.5}$$

where x_j denotes the position in various dimensions, with ω representing the turbulent frequency and k signifying turbulent kinetic energy. The parameters μ and μ_t correspond to the dynamic viscosity and turbulent viscosity of the airflow, respectively, while P_k denotes the kinetic energy production within the fluid domain. For further elucidation on the parameter configurations, readers are directed to the application of the SST $k-\omega$ model for buildings by Yang et al [46].

3.1.2 Computational Settings

The high-resolution advection scheme has been chosen to compute the advection terms within the discrete finite volume equations. Compared to both the upwind scheme and specified blend factor, this approach offers superior accuracy in resolving complex transient flow phenomena, particularly evident in regions characterized by inter-lobe and rotor tip clearances, where steep gradients manifest. Additionally, it enhances the numerical solution by preserving higher order accuracy while mitigating numerical diffusion. For transient simulations, the second-order backward scheme has been selected due to its superior accuracy in finite volume discretization. Notably, it tends to exhibit greater stability compared to the first-order backward Euler method.

The non-slip adiabatic wall boundary condition is applied to the surfaces of both rotors and stators. Given the constraints of computational resources, the simulation is limited to only half of a complete rotational cycle. Additionally, the parameters of the ideal air gas are detailed in Figure 3.1(a). To account for the real-world scenario of backflow, an opening boundary condition for both pressure and temperature is applied at the inlet and outlet, as depicted in Figure 3.1(b). Further elaboration on the specific configurations of the eight mesh cases can be found in Table 3.1.

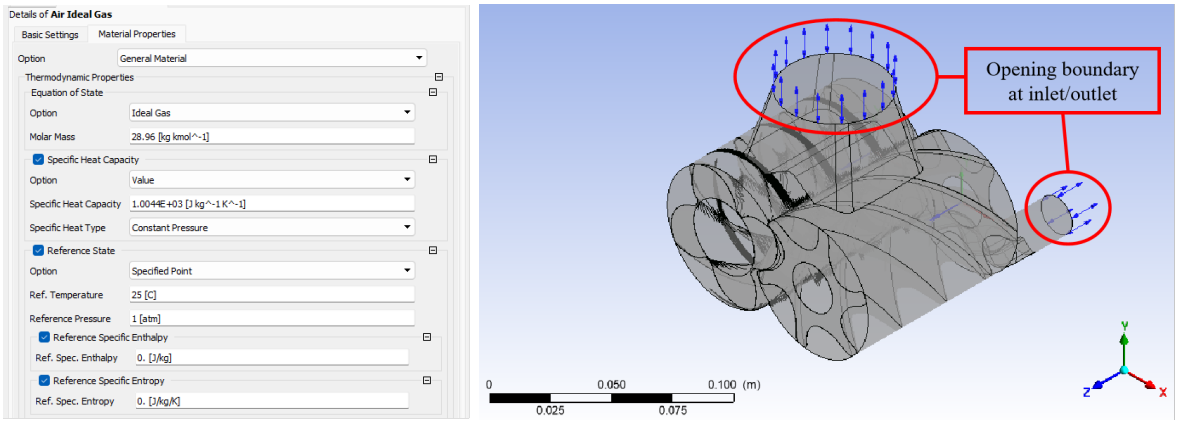

(a) parameters of the airflow (b) an opening boundary

Figure 3.1: Diagrams of detailed parameters of the ideal air gas and the opening boundary at inlets and outlets of fluid domains.

Table 3.1: Computational setting details for the single-phase airflow simulation.

Item	**Value**
Advection Scheme	High Resolution
Transient Scheme	Second Order Backward Euler
Time Step	1 degrees
Minimum Coefficient Loop	6
Maximum Coefficient Loop	8
RMS Criterion	10^{-3}
Inlet Pressure	1 bar
Inlet Temperature	298.15 K
Inlet Turbulent Intensity	5 %
Estimate Outlet Pressure	3 bar
Estimated Outlet Turbulent Intensity	Zero Gradient
Rotor Speed	3000 rpm

3.2 Mesh Independence Study

After finalizing parameter configurations for eight mesh cases in CFX-Pre, the subsequent simulations in CFX-Solver showed commendable convergence. This was validated through rigorous assessments, including residual analysis, normalised imbalance analysis and user-defined variable monitoring. Key performance indicators such as outlet temperature and outlet mass flow rate were compared across all mesh cases to identify optimal convergence conditions for meshing and simulations.

For convenience, take Mesh01 as the reference for the residual analysis, whose root mean square (RMS) criterion has been achieved well. In Mesh01, the mass RMS falls comfortably below 10^{-4}, while other RMS values are well below 10^{-3}, as illustrated in Figure 3.2. Additionally, the maximal normalized imbalance for each mesh case is collected, with all values significantly below 0.5%. The normalized imbalance, defined as the ratio of the residual imbalance of a quantity (like mass, momentum, or energy) to a reference value, indicates how well the conservation laws are satisfied within the

computational domain. The specific data together with mesh number are shown in Figure 3.3.

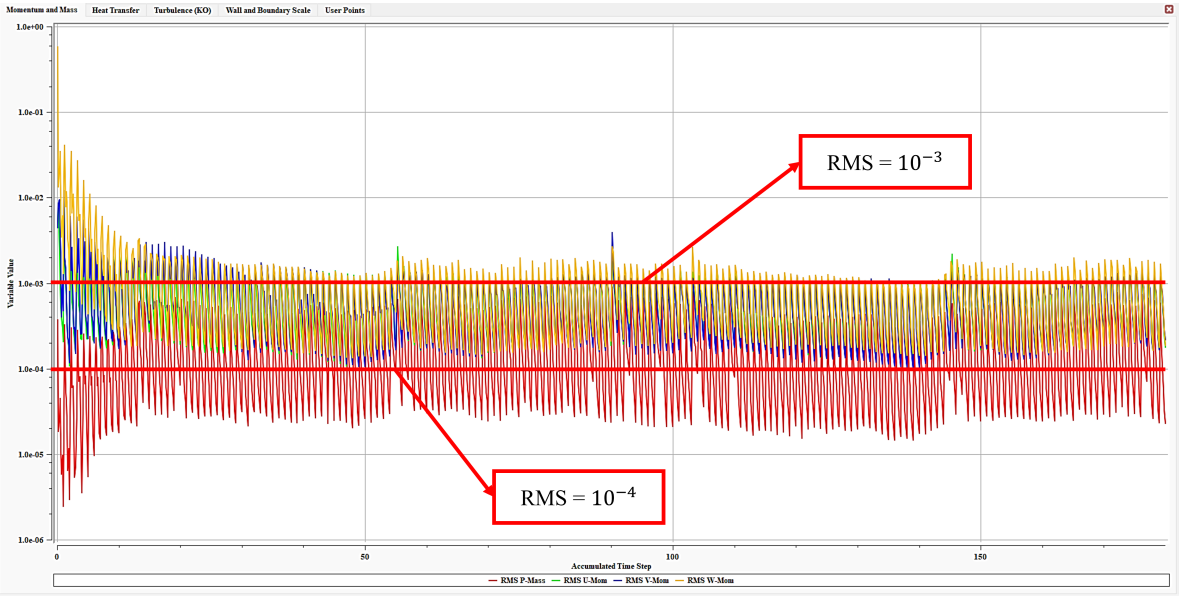

Figure 3.2: Mass and momentum RMS distribution for Mesh01 in the first half rotational cycle.

Lastly, the deviation of monitored user-defined variables from Mesh02 to Mesh08 compared with Mesh01 are calculated and sorted, whose results are shown in Figure 3.4 and Figure 3.5. The root mean square error (RMSE) method is adopted to measure the differences between referenced and practical values of monitored expression, as shown in Eq. 3.6:

$$RMSE = \frac{\sqrt{\frac{\sum_{i=m}^{n} X_i^2}{n-m+1}} - \sqrt{\frac{\sum_{i=m}^{n} Y_i^2}{n-m+1}}}{\sqrt{\frac{\sum_{i=m}^{n} X_i^2}{n-m+1}}} \tag{3.6}$$

where Y_i is the referenced value for the i_{th} data and X_i is the practical value for the i_{th} data.

According to the trends in Figures 3.4 and 3.5, mesh independence is most effectively demonstrated by Mesh01, Mesh06, and Mesh07. This indicates that increasing the maximum element size from 1mm to 1.4mm still produces a sufficiently refined grid for accurate simulation results. Mesh02 and Mesh04, despite having more circumferential

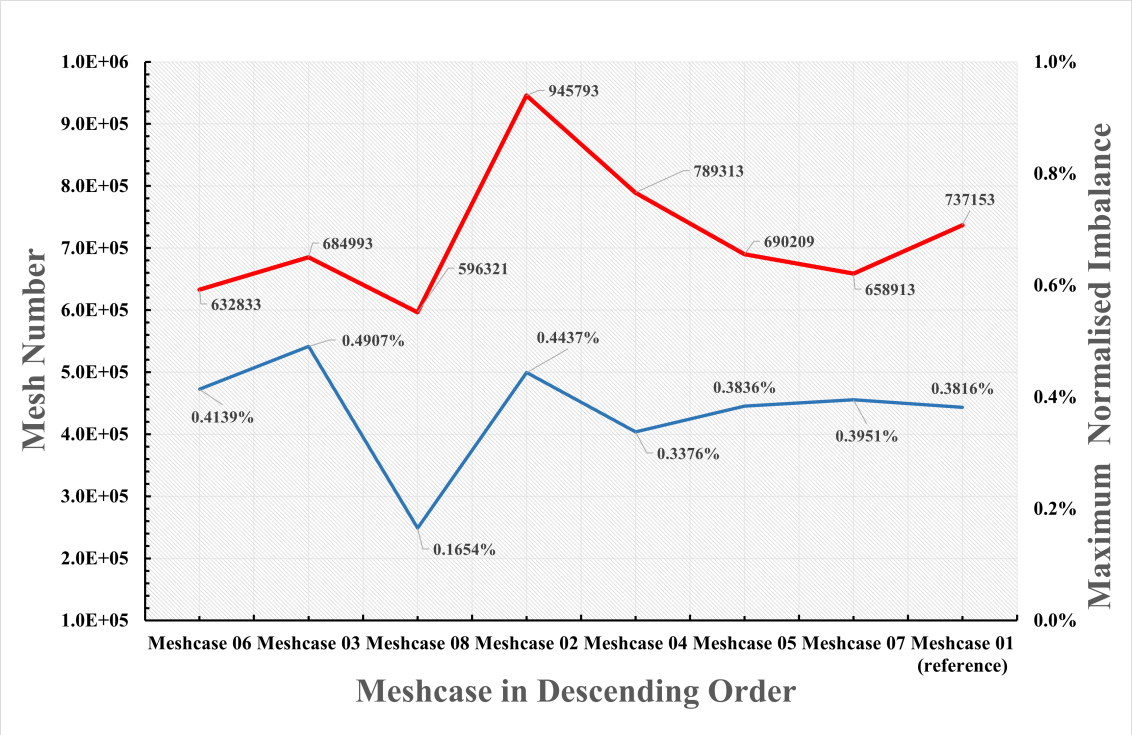

Figure 3.3: Maximal normalized imbalance and mesh number of variables in conservation equations for all mesh cases.

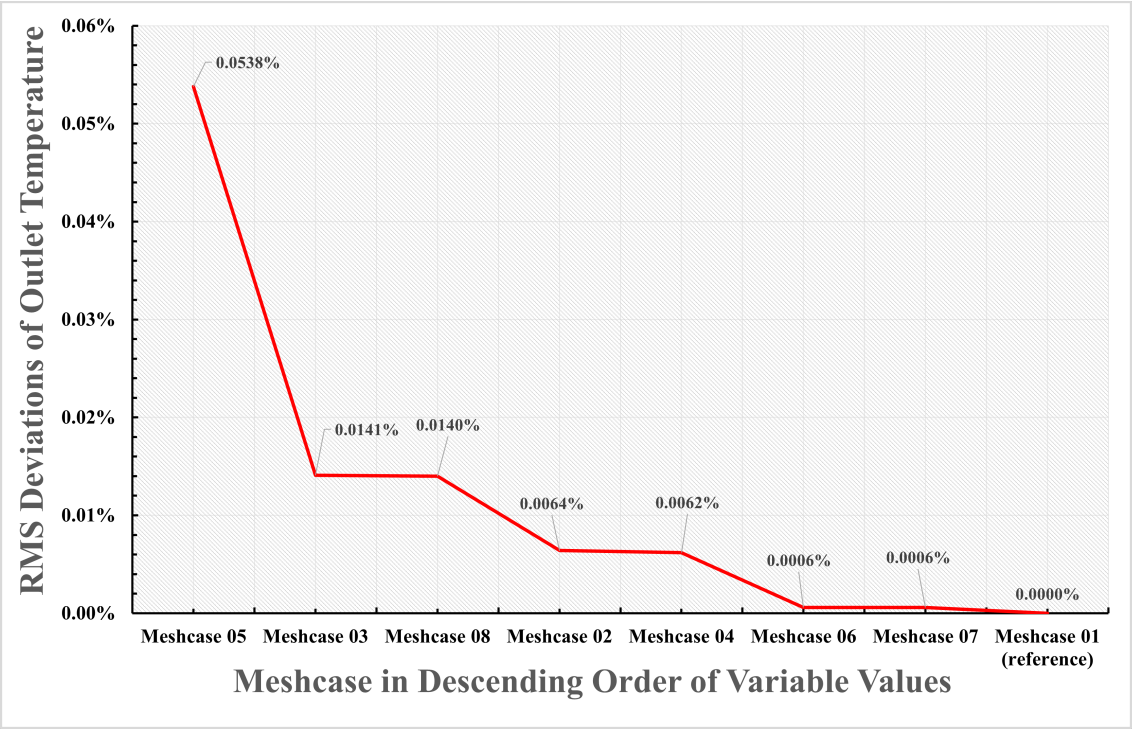

Figure 3.4: RMSE deviations of outlet temperature: differences between Mesh02-08 and reference Mesh01.

nodes, show slight deviations but remain within a satisfactory range, suggesting that 200 circumferential nodes are sufficient for accurate simulations. In contrast, Mesh03, Mesh05, and Mesh08 yield poorer results due to fewer circumferential nodes or an excessively large maximum element size, resulting in a very coarse grid. Notably, the results for Mesh05 are particularly poor, indicating that a 2mm maximum element size is too large.

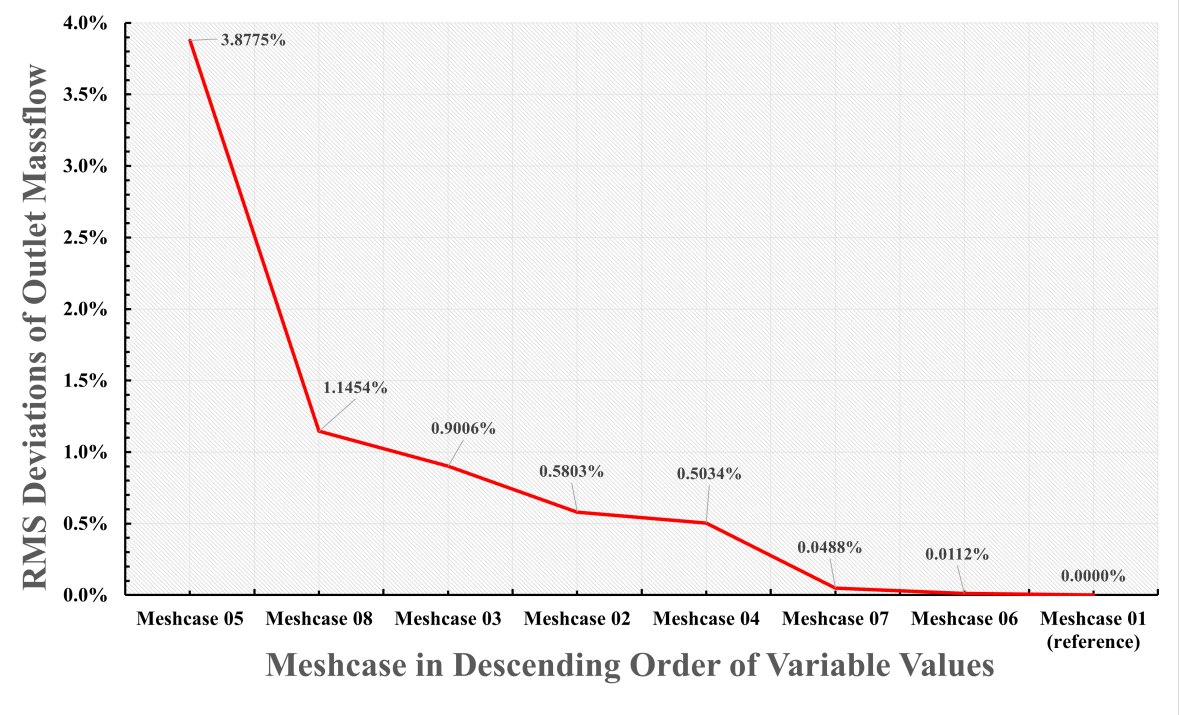

Figure 3.5: RMSE deviations of outlet mass flow: differences between Mesh02-08 and reference Mesh01.

Furthermore, the development of outlet mass flow during the compression process is depicted as fluctuating curves in Figure 3.6. The enlargement of curve tendency in purple boxes show that values of Mesh01 and Mesh07 overlap, while Mesh05 and Mesh08 deviate significantly. In Figure 3.6, a clear separation of Mesh05 from the reference Mesh01 can be observed at around 150 degrees, demonstrating that insufficient circumferential nodes greatly deteriorate simulation reliability.

In general, the mesh independence study identifies the reliability of simulation results for meshes that have the same radial, axial, and angular divisions as the reference

Mesh01, with circumferential nodes greater than 200 and a maximum element size smaller than 1.4 mm.

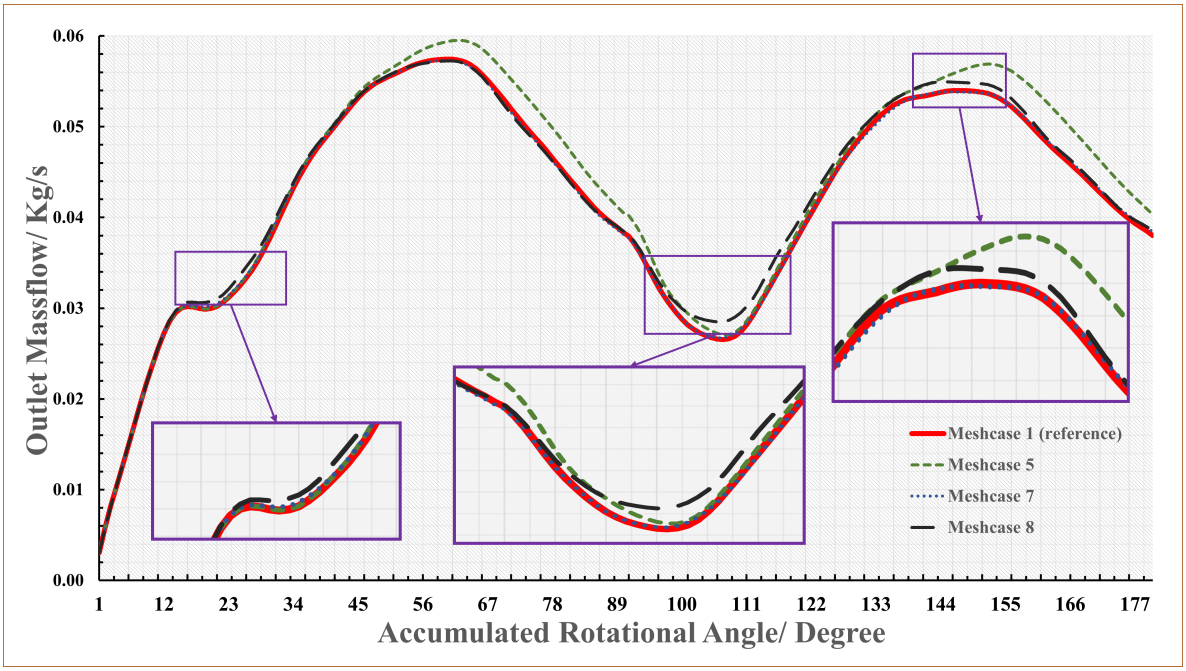

Figure 3.6: The development of outlet mass flow for different mesh cases.

3.3 Simulation Result Analysis

Pressure distribution inside the compressor is a significant indicator of its performance reliability. Consequently, pressure variations across all fluid domains of Mesh01 are recorded in Figure 3.7 for simplification, with a capture interval of 15 degrees. Among all the domains analyzed, the pressure distribution in the suction domain is the most uniform. In contrast, in the screw domain, the stratification phenomenon becomes more pronounced as the rotor rotates, consistently reaching its maximum value at the pressure outlet.

From the discharge domain, it is evident that when the rotational angle reaches 90 degrees, the outlet pressure attains the target value for the first time, after which pressure fluctuations occur, with every 90-degree rotation resulting in a pressure peak. High pressure accumulation consistently occurs at the bottom corner of the discharge

chamber, leading to uneven outlet pressure and pressure pulsation. Therefore, it is recommended to use straight discharge ports in practical production to mitigate these issues.

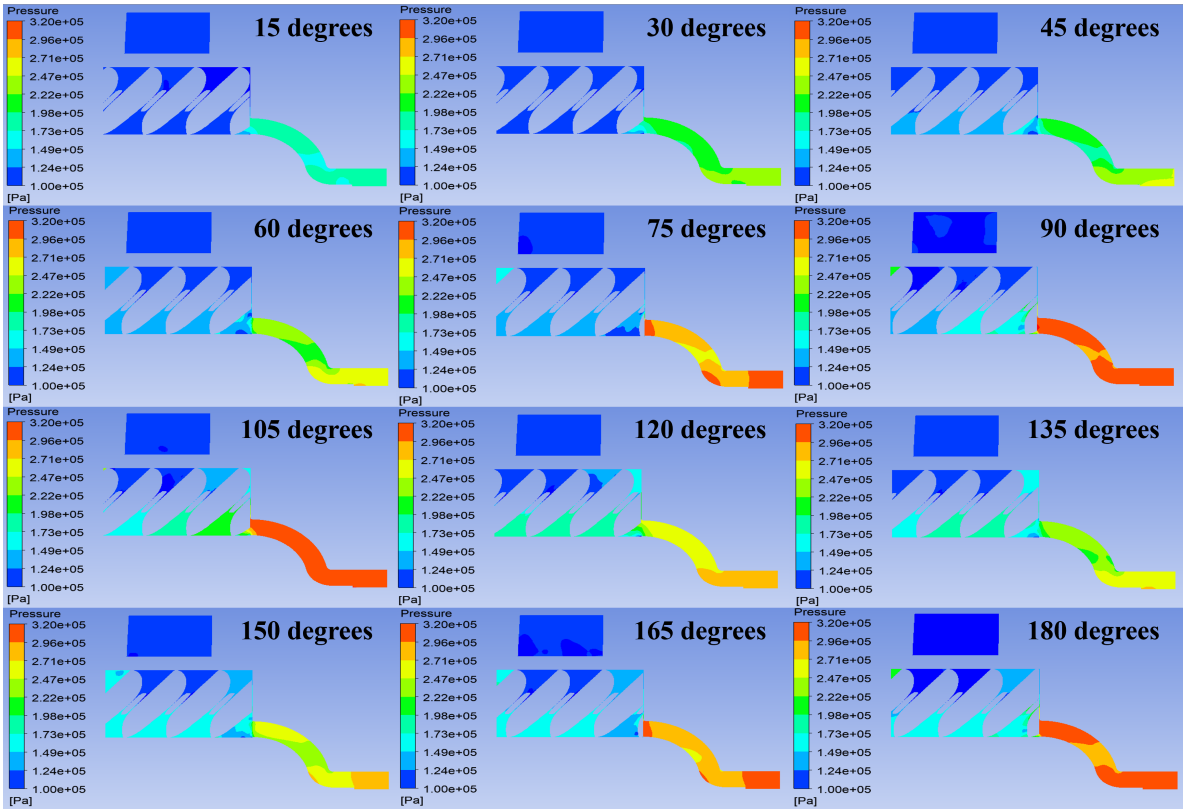

Figure 3.7: Contours of periodic variations of outlet pressure at the mid cross section for Mesh01.

To simplify the analysis, only the temperature distributions for Mesh01 and Mesh02 are represented in Figure 3.8. Their distributions are remarkably similar, proving that using 200 and 360 circumferential nodes does not significantly affect the simulation results. In the upper middle of the suction domain, an abrupt color change indicates a lower temperature, which might suggest fluid back-flow, considering that inlet boundary conditions are set to be opening. In the screw domain, the gradually increasing temperature of the airflow in the narrow inter-lobe space rises from the inlet to the outlet, reflecting excellent meshing and sealing, and indicating compressor reliability.

In the discharge domain, the temperature is smooth and consistent, except at the upper bending corners where gradients occur due to varying drift velocities. However,

the temperature increment in the simulations roughly reaches 125 degrees Celsius, which could potentially lead to excessive thermal stresses and material fatigue in the compressor, such as in rubber seals, which are neglected in the simulation. Consequently, wet compression multi-phase flow simulations of the ammonia-water mixture will be studied to try to decrease the temperature rise.

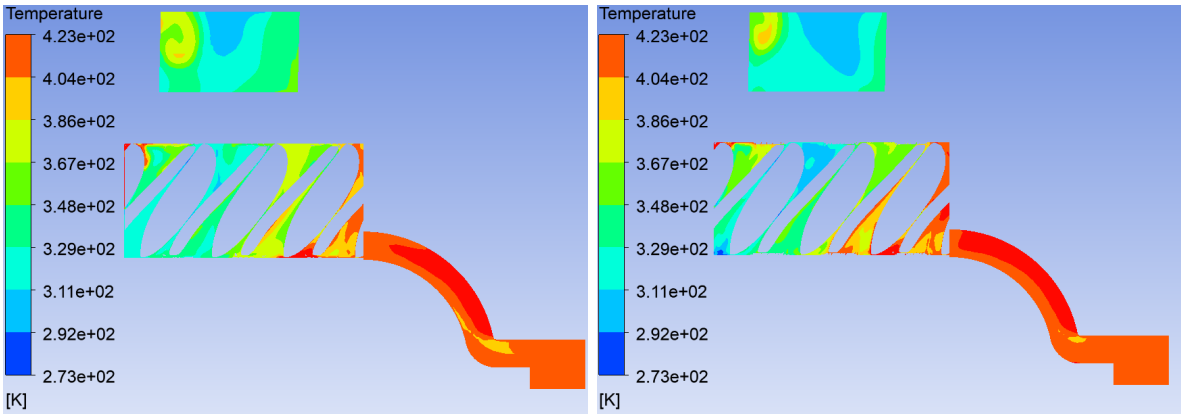

(a) Mesh01: temperature distribution (b) Mesh02: temperature distribution

Figure 3.8: Temperature distribution at the mid cross section for Mesh01 and Mesh02 at 90 degrees.

Chapter 4

Meshing and Mathematical Modelling for Multi-phase Ammonia-Water Simulations

The strategy for meshing fluid domains in complex multiphase flow simulations has undergone some changes. Key concepts introduced for this revised approach will be utilized in a mesh independence study. In the mathematical modeling section, both homogeneous and inhomogeneous models are explained, with the main difference lying in how they handle the interaction and distribution of phases within the multiphase flow. The introduction of more complex and advanced inhomogeneous models aims to make the simulation closer to real-life scenarios while incorporating necessary simplifications. Both models use the Eulerian-Eulerian method, which solves each phase individually with its own set of governing equations [47]. These governing equations together with coupled empirical turbulent closures can calculate momentum exchange between phases, as well as inter-face heat and mass forces interactions [48].

The concept of volume fraction (γ) is used to represent the relative space occupied by each phase within a single computational cell. The specified values at the inlet and outlet are based on empirical industrial applications. Physical data for ideal gaseous ammonia and liquid water are sourced from the NIST database, which are based on a

reference temperature of 25°C and a reference pressure of 1 bar. All governing equations for mass, momentum, and energy conservation, along with the heat transfer and turbulence models that separately control the behavior of ammonia and water droplets, are presented alongside the initial and boundary conditions.

4.1 Fluid Meshing under New Strategies

Multi-phase simulations with separated phases that are not mixed at mesh scales are generally numerically challenging. For instance, if the phase boundary lies within a single element, there will be very high gradients in the material properties at the vertices. The density gradient, in particular, is prone to instability or even divergence in the numerical solver. In this study, the density ratio between liquid water and gaseous ammonia is roughly 1424. As a consequence, the linear solver often fails to converge in the first coefficient loop, leading to an incorrect intermediate solution that cannot be corrected in subsequent loops. Therefore, more advanced techniques are needed to stabilize the solution, both in meshing and solver setup.

In the geometric configuration of TwinMesh, the mesh density per pitch angle is reduced from 90 to 45 to optimize computational resources. The scale value of the male rotor is increased to 100 microns, ensuring that the gap distance is adequate for the passage of water droplets. The interface generation is modified to Type 2, as this setting enhances mesh quality by positioning the interface line closer to the male rotor, particularly when a tooth of the male rotor approaches or exits a chamber of the female rotor.

In the mesh configuration of TwinMesh, the meshing type is adjusted from Mixed to Outerfix. This adjustment is made because only Outerfix allows the meshes around the male and female rotors to be glued together without requiring an interface, thereby enhancing stability. In the multi-phase simulation, radial divisions, angular divisions, and axial divisions are three major variables that affect grid quality in the mesh independence study. Radial divisions are selected to be 7, 10, and 15, considering that more than 15 elements will increase the aspect ratio, making the mesh less uniform and

deteriorating stability. The selection of axial divisions depends on the wrap angle and angular divisions, as described by the relationship in Eq. 4.1:

$$Axial\ divisions = \frac{Wrap\ angle}{Angular\ divisions} \tag{4.1}$$

therefore, 150 axial divisions correspond to a default resolution of 2 degrees. The distribution of circumferential nodes on curves is another significant variable that needs to be configured, as described by the relationship in Eq. 4.2:

$$Circumferential\ nodes = \frac{Curve\ spanned\ angle}{Angular\ division} \tag{4.2}$$

where "curve spanned angle" refers to the arc angle formed by the casing lines of the male or female components, as depicted in Figure 4.1. Proper selection ensures that the rotation increment of the rotors, which rotate beneath the mesh lines originating from the casing outline, corresponds precisely to one mesh element per time step. After completing all configurations, an initial relatively low revolution speed of 3000 rpm is adopted to validate mesh independence in the subsequent work.

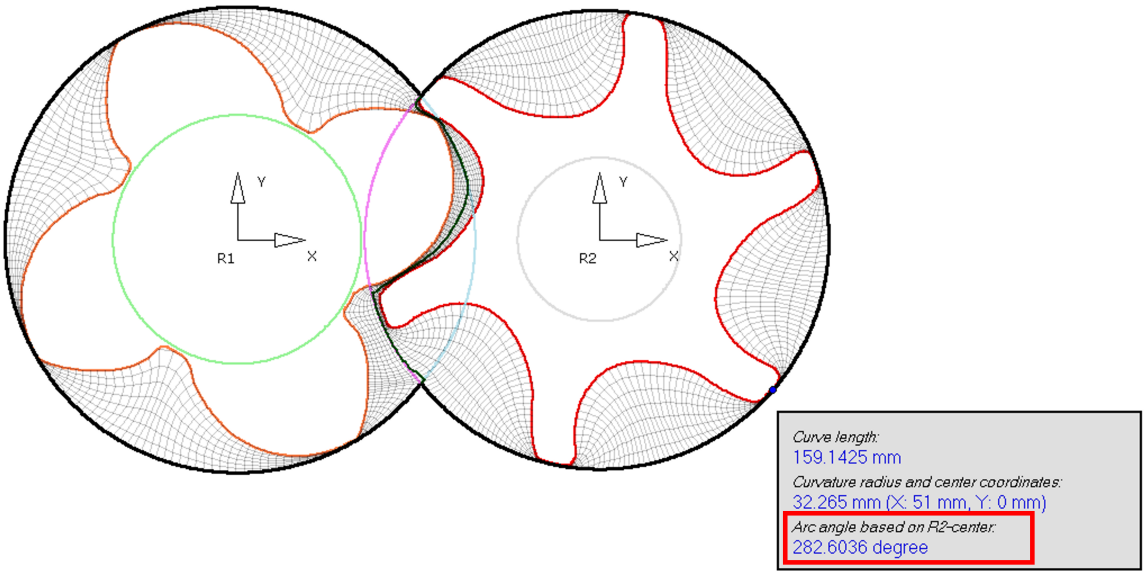

Figure 4.1: The demonstration of "curve spanned angle" for female casing line in TwinMesh.

4.2 Mathematical Modelling and Solver Settup

4.2.1 Governing Equations

Initially, the homogeneous multiphase flow model was built to perform a mesh independence study, significantly reducing computational resources and providing quick results. Although some simulated variables, such as volumetric efficiency, were not accurate enough compared to experiments conducted by Kothari [49], the model still achieved a significant boost effect and controlled the temperature rise within a reasonable range. In this model, both phases are continuous and are assumed to be well-mixed on a macroscopic scale, so the transported quantity (Φ) with the exception of rotational speed (Ω) during the compression process are the same for both phases, as shown in Eq. 4.3:

$$\Phi_\alpha = \Phi, \quad 1 \leq \alpha \leq N_P \tag{4.3}$$

where N_P is the total number of phases. Then, common fields such as velocity and temperature can be shared by both fluids. Therefore, it is sufficient to sum the individual phasic transport equations over both phases to obtain a single transport equation for Φ, as shown in Eq. 4.4:

$$\frac{\partial}{\partial t}(\rho\Phi) + \nabla \cdot (\rho \mathbf{U}\Phi - \Gamma \nabla \Phi) = S \tag{4.4}$$

where:

$$\rho = \sum_{\alpha=1}^{N_P} \gamma_\alpha \rho_\alpha$$

$$\mathbf{U} = \frac{1}{\rho} \sum_{\alpha=1}^{N_P} \gamma_\alpha \rho_\alpha \mathbf{U}_\alpha \tag{4.5}$$

$$\Gamma = \sum_{\alpha=1}^{N_P} \gamma_\alpha \Gamma_\alpha$$

On the other hand, the inhomogeneous model has been used for performance im-

provement. This model treats the governing equations for the continuous ammonia phase (α) and the discrete water phase (β) separately. In this study, a particle model is utilized for interfacial transfer. The surface area per unit volume $A_{\alpha\beta}$, is obtained by assuming that β consists of spherical particles with a mean diameter d_β, as shown in Eq. 4.6. The continuity equation for the continuous phase is presented in Eq. 4.7:

$$A_{\alpha\beta} = \frac{6\gamma_\beta}{d_\beta} \tag{4.6}$$

$$\frac{\partial \rho_g}{\partial t} + \nabla \cdot (\rho_g \boldsymbol{u}_g) = S_g \tag{4.7}$$

where ρ_g is the density of the ammonia gas, t is the computational time, $\boldsymbol{u}_g$ is the velocity vector of the gas phase, S_g is the source term representing mass transfer between phases. In addition, the continuity equation for water droplets is often described by tracking the number density function $n_d(\boldsymbol{x}, \boldsymbol{v}, t)$ of the droplets, where $\boldsymbol{x}$ and $\boldsymbol{v}$ are the position and velocity of the droplets, which is presented in Eq. 4.8:

$$\frac{\partial n_d}{\partial t} + \nabla_{\boldsymbol{x}} \cdot (n_d \boldsymbol{v}) + \nabla_{\boldsymbol{v}} \cdot (n_d \boldsymbol{a}) = \tilde{S}_d \tag{4.8}$$

where $\boldsymbol{v}$ is the velocity of droplets, $\boldsymbol{a}$ is the acceleration of droplets, $\tilde{S}_d$ is a source term which includes droplet breakup, coalescence, and mass transfer between phases. Furthermore, the term $\nabla_{\boldsymbol{x}} \cdot (n_d \boldsymbol{v})$ represents the spatial transport of droplets due to their motion, and the term $\nabla_{\boldsymbol{v}} \cdot (n_d \boldsymbol{a})$ accounts for the changes in droplets' velocity due to forces acting on them. For momentum conservation, the Schiller-Naumann model is specifically adopted for the primary drag force between phases. For simplification, non-drag forces are set to their default options. The momentum equation for the ammonia gas is presented in Eq. 4.9:

$$\begin{aligned} &\frac{\partial (\rho_g \mathbf{u}_g)}{\partial t} + \nabla \cdot (\rho_g \mathbf{u}_g \mathbf{u}_g) = -\nabla p + \nabla \cdot (\tau_g) + \rho_g \mathbf{g} + \mathbf{F}_g \\ &\mathbf{F}_g = \frac{1}{V} \sum_i \mathbf{F}_{drag,i} \end{aligned} \tag{4.9}$$

where p is the pressure of the ammonia gas and τ_g is the stress tensor accounting for viscous forces. The interaction force $\mathbf{F}_g$ between the ammonia gas and the droplets can be derived from the summation of the forces acting on all droplets within a computational control volume. Besides, the momentum equation for each individual droplet is written in Eq. 4.10:

$$\begin{aligned} m_d \frac{d\mathbf{u}_d}{dt} &= m_d \mathbf{g} + \mathbf{F}_{drag} + \mathbf{F}_{other} \\ \mathbf{F}_{drag} &= \frac{1}{2} C_d \rho_g A_d (\mathbf{u}_g - \mathbf{u}_d)|\mathbf{u}_g - \mathbf{u}_d| \end{aligned} \tag{4.10}$$

where m_d is the mass for water droplet and $\mathbf{F}_{drag}$ is due to the relative motion between droplet and the gas. For this drag force, C_d is the drag coefficient, A_d is the cross-sectional area of the droplet and $(\mathbf{u}_g - \mathbf{u}_d)$ is the relative velocity. In addition, a homogeneous total energy model, which simplifies the heat transfer process and does not consider the interfacial transfer effect, is utilized as shown in Eq. 4.11:

$$\begin{aligned} &\frac{\partial(\rho_g e_g)}{\partial t} + \nabla \cdot (\rho_g e_g \boldsymbol{u}_g) = -p_g(\nabla \cdot \boldsymbol{u}_g) + \nabla \cdot (k_g \nabla T_g) + \dot{Q}_{g\to d} + \dot{Q}_g \\ &\frac{d}{dt}\left(\sum_i m_{d,i} e_{d,i}\right) = \sum_i \left(\dot{Q}_{g\to d,i} + \dot{Q}_{d,i}\right) \end{aligned} \tag{4.11}$$

where e_g denotes the specific internal energy of the ammonia gas, T_g represents the temperature of the gas, and k_g is the corresponding thermal conductivity. Specifically, $\dot{Q}_{g\to d}$ accounts for the interphase heat transfer from the ammonia gas to the water droplets, while $\dot{Q}_{d,i}$ represents any other heat sources or sinks in the gaseous phase. For the droplet energy change equation, $\frac{d}{dt}\left(\sum_i m_{d,i} e_{d,i}\right)$ indicates the temporal change of the total internal energy of the droplets, and $\sum_i \left(\dot{Q}_{g\to d,i} + \dot{Q}_{d,i}\right)$ represents the summation of the heat transfer rates and any other heat sources within the droplets. Moreover, the turbulent model is fluid-dependent. For the ammonia gas, the traditional SST model is used, which is suitable for high-speed and compressible wall heat transfer scenarios, as reviewed in Eq. 3.2. For the water droplets, the dispersed phase zero-equation model

is adopted, mainly focusing on estimating the turbulent dispersion force $\boldsymbol{F}_{td}$ and the turbulent kinetic energy k_d, as shown in Eq. 4.12:

$$\begin{aligned} \boldsymbol{F}_{td} &= -C_{td}\rho_g k_g \nabla \alpha_d \\ k_d &= C_k k_g \end{aligned} \tag{4.12}$$

where C_{td} is a model constant, k_g is turbulent kinetic energy of ammonia gas, and $\nabla\alpha_d$ is the gradient of the volume fraction of water droplets. Note that for the zero-equation model, only simplified algebraic equations are used to evaluate the turbulent effect, without involving solving additional transport equations.

4.2.2 Solver Setup

In general, material properties, solver control methods, boundary conditions, and initial conditions are the four main domains that primarily control the accuracy and stability of solvers. Given that the detailed settings differ for mesh independence studies and model accuracy validation compared with Marina's model, an outline is provided in this section. More specific settings, such as volume fraction and rotational speed, can be found in each section of the next chapter.

Properties of water droplets primarily come from NIST, assuming that water density remains unchanged during compression. For ammonia, properties are either obtained from NIST or deduced using the ideal gas equation of state. Specific pressure and temperature are required in the suction domain, and these properties are highly sensitive to changes, as illustrated in Figure 4.2. In addition, the average diameter of the water droplets d_β is determined via the Sauter Mean Diameter (SMD), which is an average measure of particle size in multiphase flows in Eq. 4.13:

$$SMD = \kappa \left(\frac{\sigma}{\rho_d u^2} \right)^{0.6} d^{0.4} \tag{4.13}$$

where ρ_d is the density of water, u is the relative velocity between two phases, σ is the interfacial tension of the water, κ is an empirical constant typically found through

experimental data, d is the characteristic length scale of the compressor. Detailed values are collected in Table 4.1 in SI. After calculation, d_β is approximated as 10 microns. Besides, the solver control method "First Order Backward Euler" transient scheme is adopted to ensure stability. A minimum pressure of 10,000 Pa is set to avoid very low ammonia densities in cases where the pressure is very low.

Table 4.1: Values of variables selected for calculations of average water droplet diameter.

Term	κ	u	ρ_d	σ	d
Value	0.25	20	997	0.0728	0.086

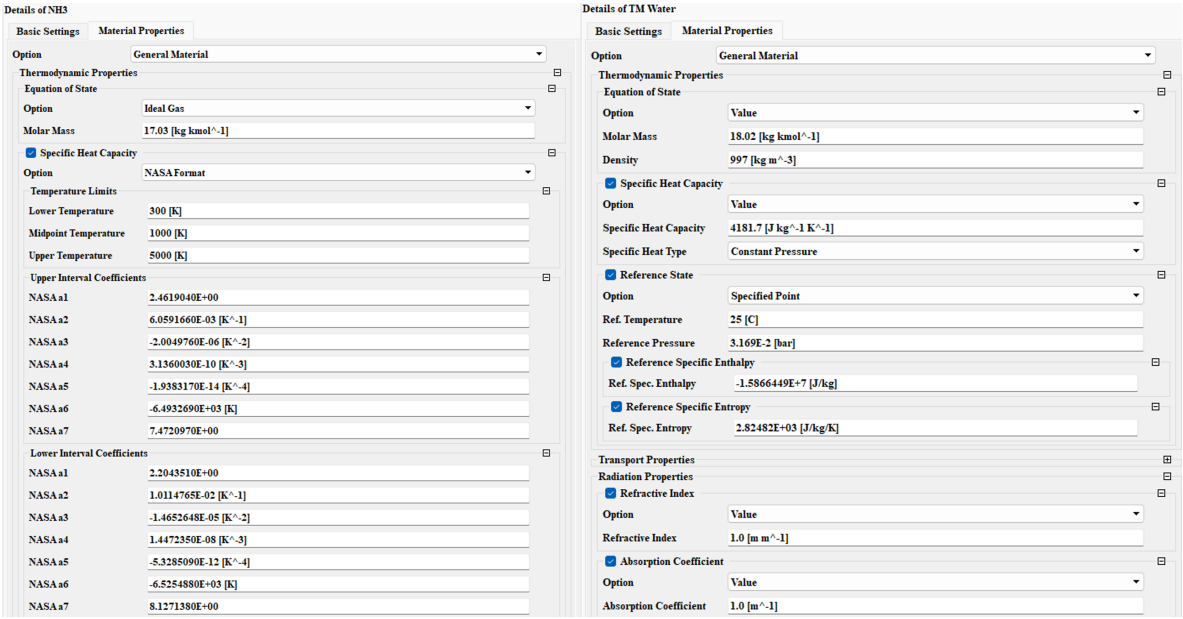

Figure 4.2: Material properties and ammonia and water when temperature and pressure are 298.15K and 1bar respectively.

Chapter 5

Simulation Results Analysis with Return Flow Included

Leakage of working fluids inside twin-screw compressors, a tricky problem in the industry, has not been discussed in previous chapters. Many researchers neglect this phenomenon or treat it simply [49]. One outstanding method for alleviating leakage is the use of gap seals, such as labyrinth seals or contact seals, which direct the flow inside the seals at the high-pressure discharge domain back to the suction domain of the compressor. Marina has conducted extensive research on this topic using MATLAB simulations to investigate the effect of gap seals on the efficiency and performance of a similar compressor model. In this study, more complicated and realistic CFX models will be constructed to validate Marina's outcomes and investigate how indicators such as pressure distribution and power consumption are affected by gap seals.

Initially, a mesh independence study for various multiphase flow simulations is conducted, examining how coarsened radial divisions, angular resolution, and axial division affect simulation accuracy. Typically, there are thresholds for these variables below which grid quality is unsatisfactory. Next, the advantages of the inhomogeneous model compared with the homogeneous one are validated in Kothari's model, which has a tight connection with Marina's model [49]. Finally, a return flow pipeline is connected between the inlet and outlet to simulate the gap seal effect. This returning flow, having

the same thermodynamic properties such as vapor quality and pressure as the discharge flow, will influence the inlet flow mixtures. Its impact on the performance of the compressor, as well as the physical fields inside the pipeline, is analyzed and compared with Marina's results.

5.1 Mesh Independence Study

The homogeneous model with separate ammonia and water inlets is used for the mesh independence study, saving computational resources while ensuring result reliability. The model is shown in Figure 5.1. Information about the initial and boundary conditions of the study, such as the pressure ratio (PR), as well as the list of variables being investigated, are provided in Table 5.1 and Table 5.2.

Table 5.1: Values of variables for the setup of mesh independence study.

Term	P_{in} [bar]	T_{in} [K]	γ_{NH_3}	PR	Ω [rpm]
Value	1	298.15	0.98	3	3000

Table 5.2: A list of mesh cases and their variable ranges for mesh independence study.

Case	**Radial Division**	**Resolution [°]**	**Axial Division**	**Mesh Number**
Mesh01	15	2	150	1,600,329
Mesh02	10	2	150	1,189,929
Mesh03(reference)	7	2	150	943,689
Mesh04	15	2.5	120	1,204,409
Mesh05	7	2.5	120	724,049
Mesh06	7	2.5	90	649,409
Mesh07	7	1.5	200	1,391,839

The introduction of angular resolution is the main difference from the single-phase mesh independence study. In single-phase cases, the mesh quantity isn't as massive as in multi-phase flow; therefore, a 1-degree refined resolution is used for all mesh cases. The mixture of ammonia and water increases the complexity of the system, requiring a

relatively low resolution that still ensures a refined grid. Because the angular resolution varies for some cases, the data for each time step cannot be compared directly. Sampling is required to make data comparisons at the same rotational position, meaning only 36 sampling points are needed for one complete rotation (mesh cases with 2 and 2.5 degrees resolution result in a sampling frequency of 10 degrees.). The comparison of outlet pressure, outlet temperature and mass flow rate for all cases are shown in Figures 5.2, 5.3, and 5.4. For each comparison, differences of all variables among Mesh01, Mesh02, Mesh03 and Mesh07 are approximate, demonstrating two outcomes: the individual increase of radial division from 7 to 15 won't affect results; the coarsening of resolution from 1.5 to 2 degrees won't make results worse.

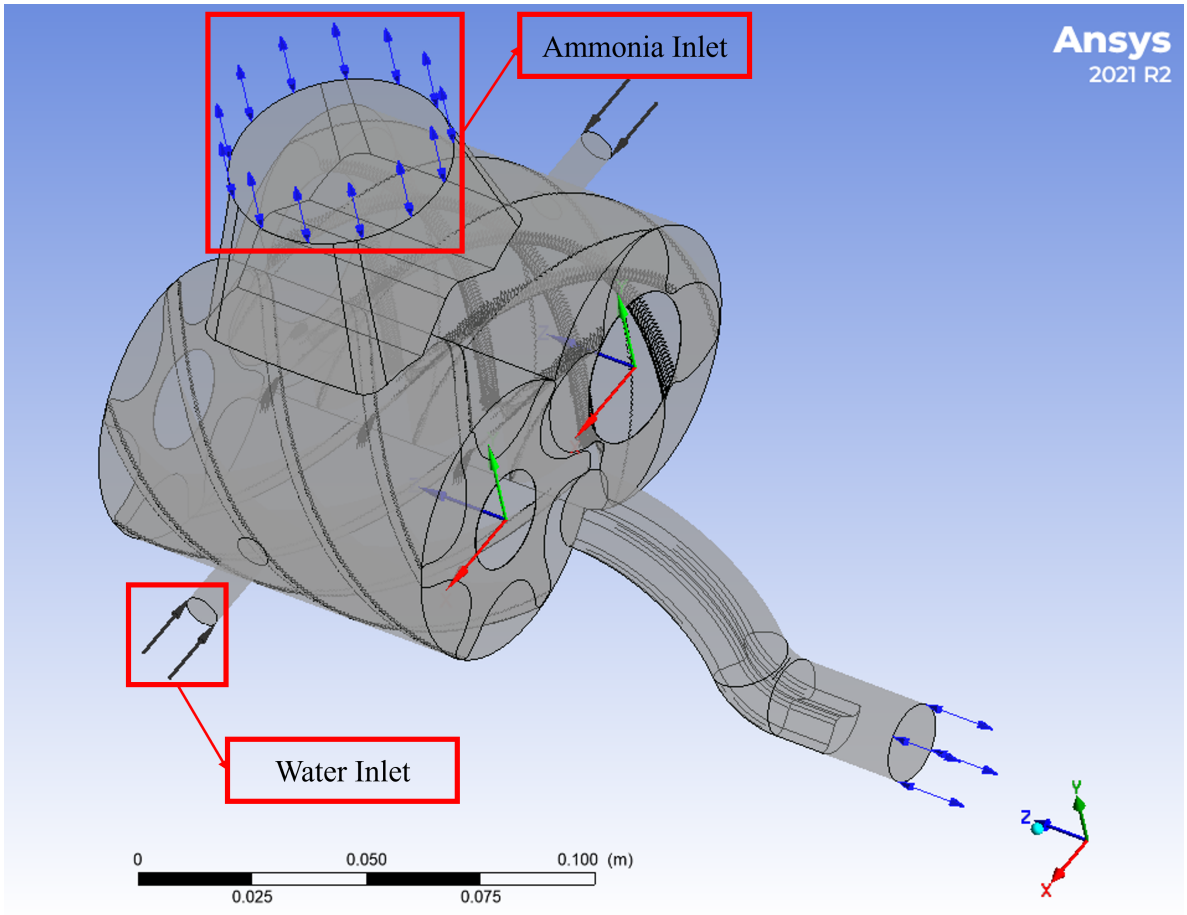

Figure 5.1: The demonstration of the homogeneous compressor model with ammonia and water inlets being separate.

When the angular resolution is increased to 2.5 degrees in Mesh04, Mesh05, and

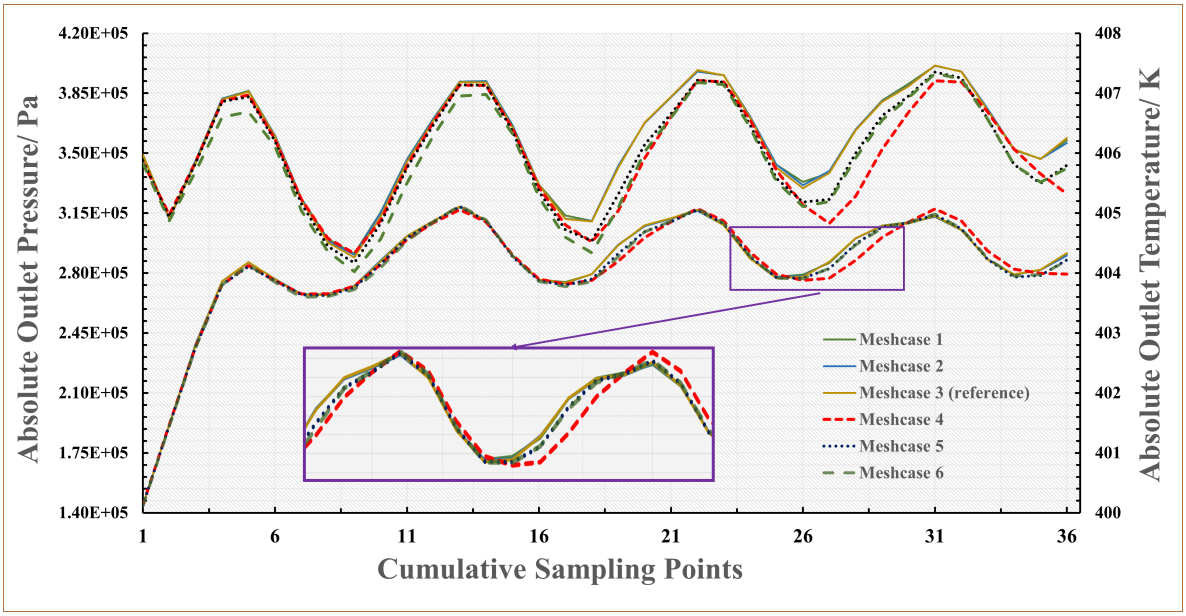

Figure 5.2: Comparison of outlet pressure and temperature for mesh cases of 2.5 and 2 degree resolution.

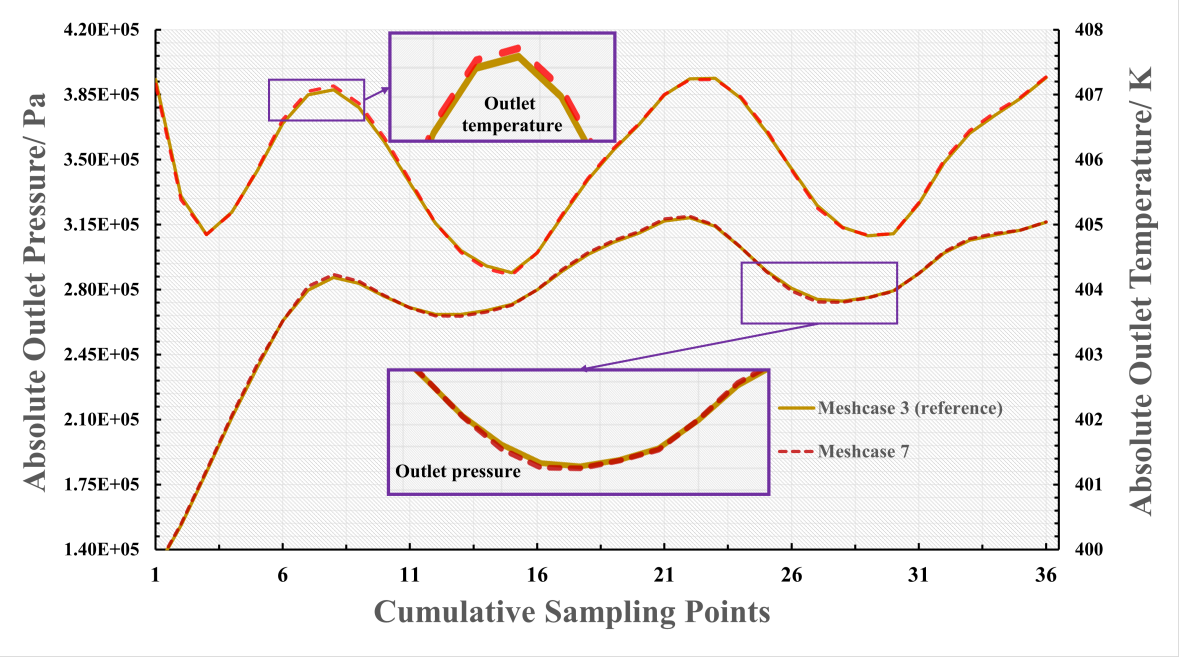

Figure 5.3: Comparison of outlet pressure and temperature for mesh cases of 1.5 and 2 degree resolution.

Mesh06, the results deviate significantly from the reference, particularly for Mesh04 and Mesh06. This indicates that excessive radial division or insufficient axial division, combined with coarser resolution, are inadvisable. In summary, Mesh02 or Mesh03 are recommended for further investigation of backflow effects on compressor performance. Detailed deviations from Mesh03, using the RMSE method, are listed in Table 5.3.

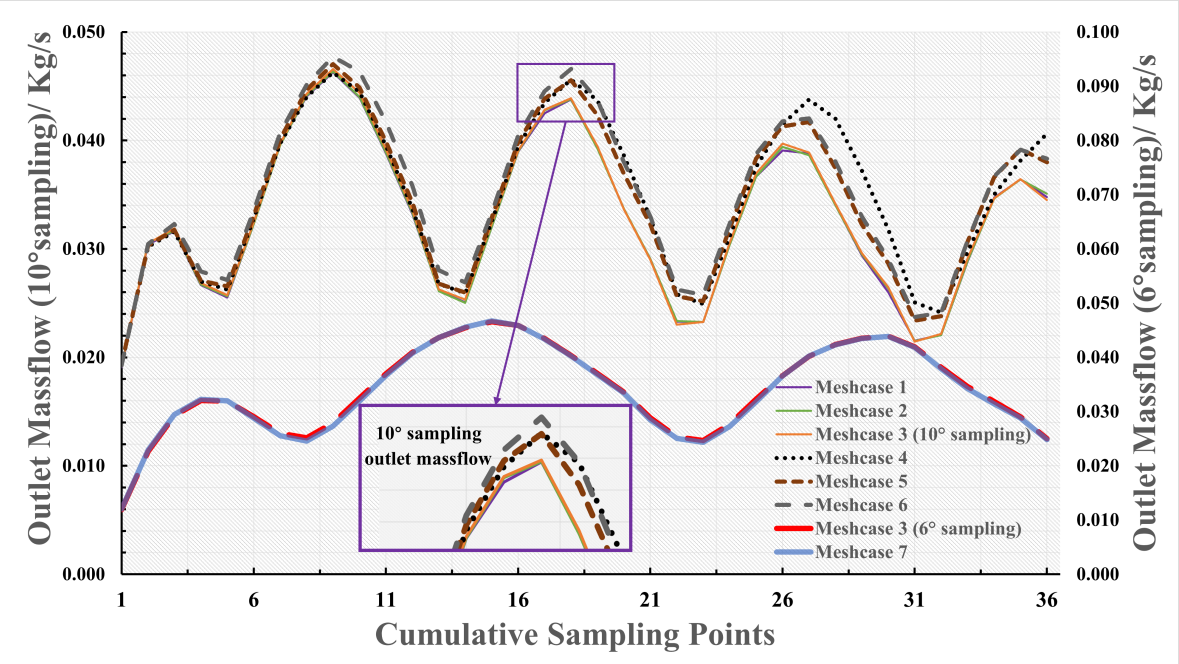

Figure 5.4: Comparison of outlet mass flow rate for mesh cases of all resolutions.

Table 5.3: RMSE deviations of all variables for all meshes compared with reference Mesh03

Case	Mesh01	Mesh02	Mesh04	Mesh05	Mesh06	Mesh07
Pressure [%]	0.015	0.006	0.518	0.402	0.491	0.117
Temperature [%]	0.005	0.003	0.054	0.042	0.067	0.002
Mass flow [%]	0.517	0.362	5.255	4.200	6.119	0.431

5.2 Model Optimization Comparison

The rotational speed in Kothari's experiments varies between 9030 rpm and 14205 rpm, and the range of PR is from 1.9 to 3.3. The inlet vapor quality for each data set is well recorded, while the experiment does not consider the gap seal. For simplification, it is assumed that the mixture at the inlet is composed solely of ammonia vapor and water liquid, without considering ammonia being dissolved in the water. Therefore, the volume fraction for each component can be calculated from the vapor quality via ideal gas equations. Additionally, in Kothari's experiments, the discharge temperature is manually limited to the range of 110-120 degrees Celsius to avoid the accumulation of fouling on the water side of the absorber at higher temperatures. Eq. 5.3 is useful for estimating the inlet temperature, considering the assumption of ideal ammonia and a low water volume fraction. Further, the values of volumetric efficiency and discharge temperature for each case are shown in Figure 5.5, where triangles represent Kothari's experiment, while circles represent Marina's model.

$$T_{out} = T_{in} \cdot (P_{out}/P_{in})^{0.4/1.4} \tag{5.1}$$

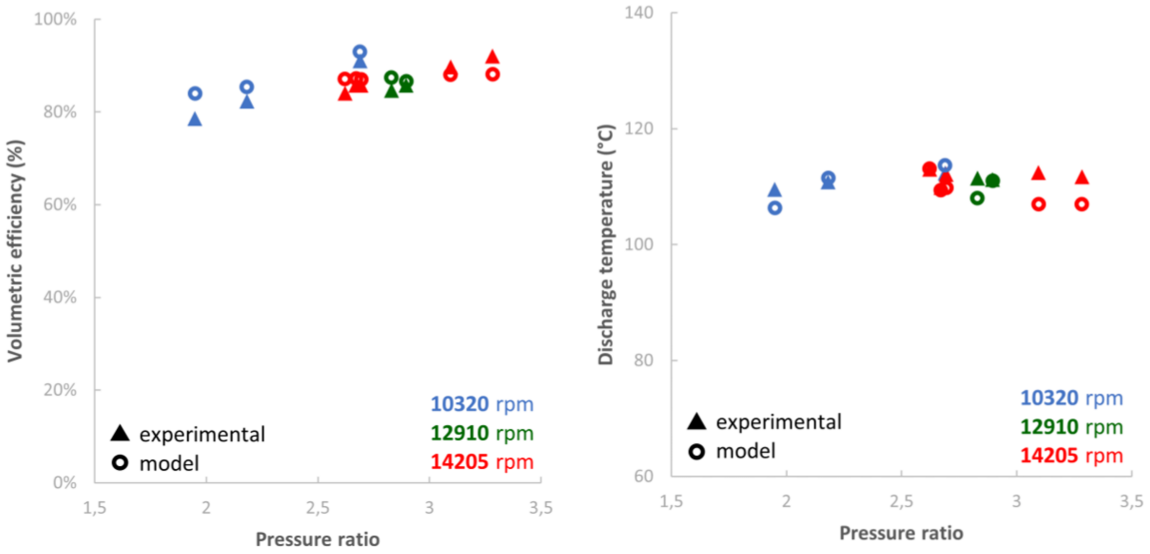

Figure 5.5: Volumetric efficiency and discharge temperature in Kothari's and Marina's models for all cases.

Then, boundary conditions for determining thermodynamic states of the mixture at suction and discharge domains for Kathari's experiments and this study are summarized in Table 5.4 and Table 5.5, respectively. In addition, the volumetric efficiency (η_{vol}) for the simulated model is determined by inlet mass flow rate (Q_{in}), inlet average density ($\bar{\rho_{in}}$) and theoretical total volume flow rate (Q_{tot}), whose relation is showm in Eq. 5.2.

Table 5.4: The boundary conditions in Kathari's experiments for the inhomogeneous model validation.

Case	P_{in} [bar]	T_{out} [K]	γ_{NH_3} [%]	PR	Ω [rpm]
01	1	385.15	99.98	2.7	10320
02	1	383.15	99.95	3.0	12910
03	1	385.15	99.94	3.3	14205

Table 5.5: The boundary conditions in this research for the inhomogeneous model validation

Case	P_{in} [bar]	T_{in} [K]	γ_{NH_3} [%]	PR	Ω [rpm]
01	1	293.15	99.98	2.7	10320
02	1	283.15	99.95	3.0	12910
03	1	276.15	99.94	3.3	14205

$$\begin{aligned} \eta_{vol} &= Q_{in}/\bar{\rho_{in}}/Q_{tot} \\ Q_{tot} &= V_{tot} \cdot \Omega \end{aligned} \tag{5.2}$$

The general performance of the homogeneous model is not satisfactory, as evidenced by the significant discrepancies compared to real experimental values. Among the three inhomogeneous simulations, Case02 exhibits the largest difference, approximately 8.9% smaller. However, it still does not match very closely due to the lack of evaporation simulation in the inhomogeneous model. In real experiments, the evaporation of water droplets absorbs a significant amount of latent heat, lowering the overall temperature inside the compressor. Cooler gas occupies less space at a given pressure, allowing more

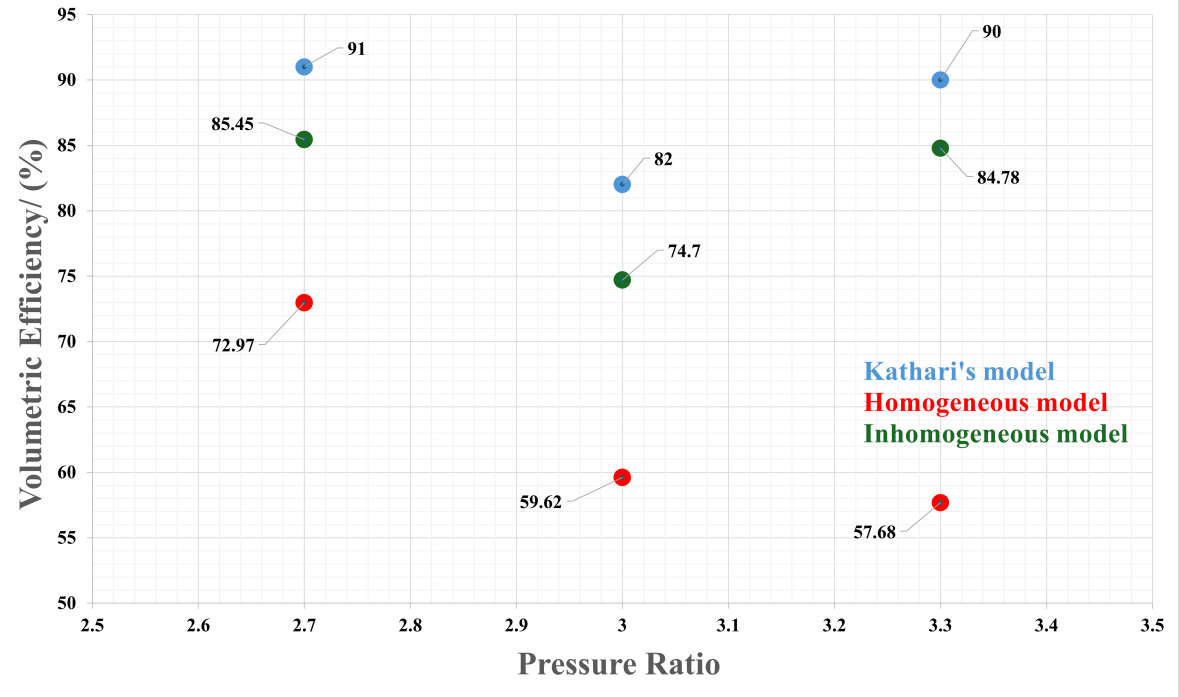

Figure 5.6: Results of volumetric efficiency versus varied boundary conditions between models and experimental data.

gas to be drawn in during the intake stroke. Adding an evaporation feature would make the system too complex and resource-intensive, so it is omitted in this study. In general, the range of difference is between 6% and 9%, demonstrating that the updated model is useful for further study on the gap seal effect.

5.3 Gap Seal Modelling

In general, leakages inside compressors from the discharge domain to the suction domain can be partially mitigated by incorporating a gap seal. This seal facilitates a backflow, which helps to alleviate excessive flow burden at the outlet, as illustrated in Figure 5.7. The ideal mass flow rate through the seal can be estimated using the nozzle flow equation, given in Eq. 5.3:

$$\dot{m_{seal}} = C_{seal} \cdot \sqrt{2\rho_{seal}(P_{dis} - P_{suc})} \tag{5.3}$$

where $\dot{m}_{seal}$ denotes the mass flow rate through the seal. C_{seal} is an experimental flow coefficient that depends on the cross-sectional area, length scale, and inner wall friction coefficient of the seal. ρ_{seal} is the density of the mixture inside the seal, which varies based on the volume fraction of each component within the seal.

This section examines the impact of the mass flow from the gap seal on compressor performance metrics such as volumetric efficiency, compressor power consumption, and overall fluid distribution. The statistical results from each case need to be compared with data from Marina to assess how closely our model results align, considering that the primary physical parameters of the twin-screw compressors we have built are similar. Furthermore, contours of fluid property distributions at cross sections of whole fluid domains are analysed to see how the addition of gap seal changes physical fields.

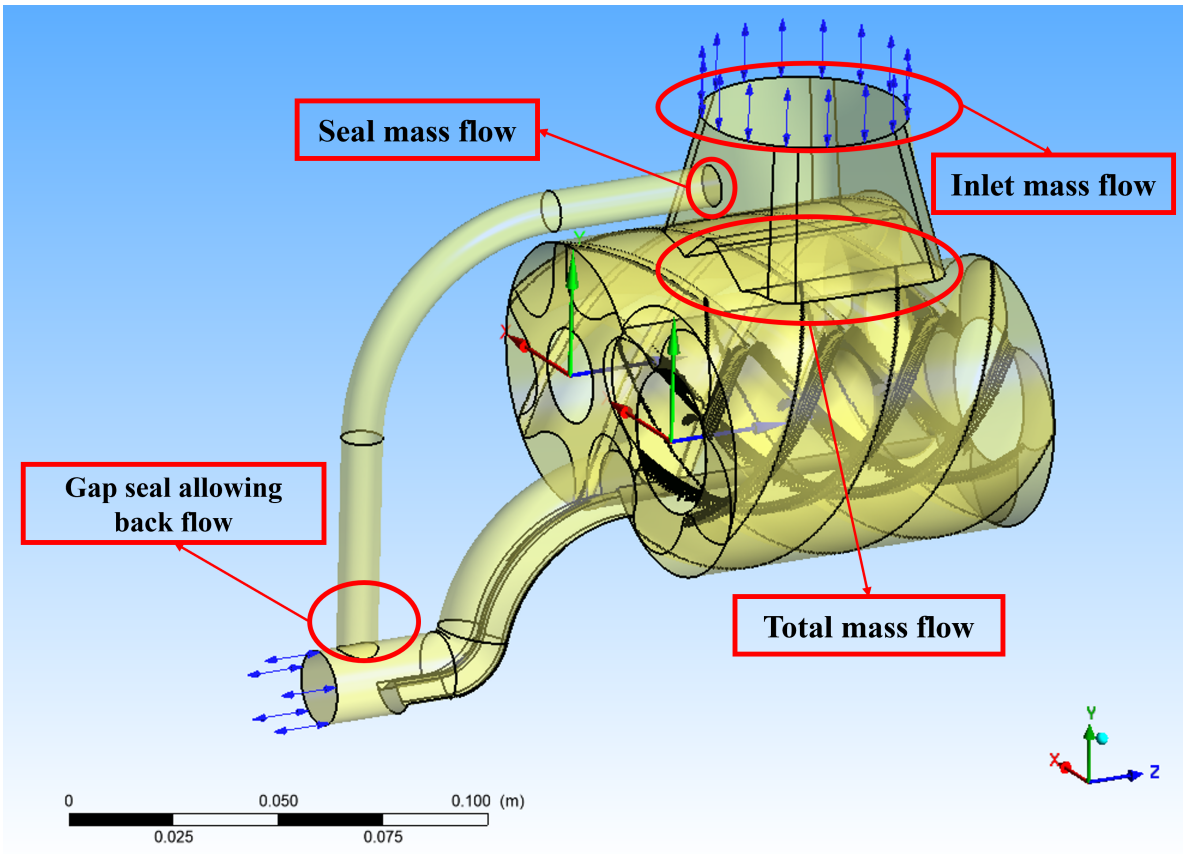

Figure 5.7: The appearance of the simulated compressor with the gap seal included.

Initially, the data used for the boundary conditions of the serial simulations is listed in Table 5.6. During the investigation, all conditions are kept constant throughout the

entire fluid domain, except for the suction domain where the mixture of $\dot{m_{seal}}$ and $\dot{m_{in}}$ occurs. The concept of seal mass fraction (ψ) is defined as the percentage of the mass flow through the seal relative to the total mass flow at the entrance of the rotor, as shown in Eq. 5.4.

Table 5.6: Boundary conditions for gap seal simulations.

Term	P_{in} [bar]	T_{in} [K]	γ_{NH_3}	PR	Ω [rpm]
Value	2	351.65	0.999	3	10320

$$\dot{m_{tot}} = \dot{m_{seal}} + \dot{m_{in}}, \quad \psi = \frac{\dot{m_{seal}}}{\dot{m_{tot}}} \tag{5.4}$$

The inlet and outlet mass flows should normally be balanced, whether for the fluid domains of the entire compressor system or solely for the gap seal, after sufficient iteration time steps. This balance is a significant indicator of mass conservation and simulation convergence, alongside the residual analysis of governing equations and maximum imbalance monitoring. The averaged mass flows at global inlets and outlets, as well as those of gap seals, are recorded in Table 5.7. These values result from RMS calculations, eliminating undesired pulsations. Importantly, data from the initial 45 time steps are not considered, as flow patterns are weak and the flow rate is chaotic at the beginning.

Table 5.7: The data for averaged mass flows at the global inlet and outlet of the compressor as well as the gap seal pipeline.

Term	$\bar{m_{tot,in}}$ [Kg/s]	$\bar{m_{tot,out}}$ [Kg/s]	$\bar{m_{seal,in}}$ [Kg/s]	$\bar{m_{seal,out}}$ [Kg/s]	ψ [%]
Case01	0.0686	0.0684	0	0	0
Case02	0.0843	0.0835	0.0163	0.0159	19.33
Case03	0.1085	0.1104	0.0456	0.0446	42.03

Averaged mass flow rates, rather than instantaneous values, are used for convergence analysis in the steady state. This approach accounts for the returning mass flows at the global inlet and outlet of the compressor, caused by periodic pressure fluctuations. Note

that there are three simulation cases in total, with ψ in ascending order. Furthermore, the addition of $\bar{m_{in}}$ in Case01 and $\bar{m_{seal,in}}$ in Case02 or Case03 yields $\bar{m_{tot,in}}$ in the corresponding cases. This is equivalent to the constant mass flow at the global inlet for all three cases. This observation stems from the fact that the boundary conditions set beforehand are the same for all three simulations. Consequently, the average inlet mass flows remain constant, even though the instantaneous inlet mass flows can vary initially due to the presence of gap seals with different seal diameters. Additionally, the accumulated mass flows for gap seals are represented in Figure 5.8, illustrating that after a certain number of time steps, the flow becomes stable.

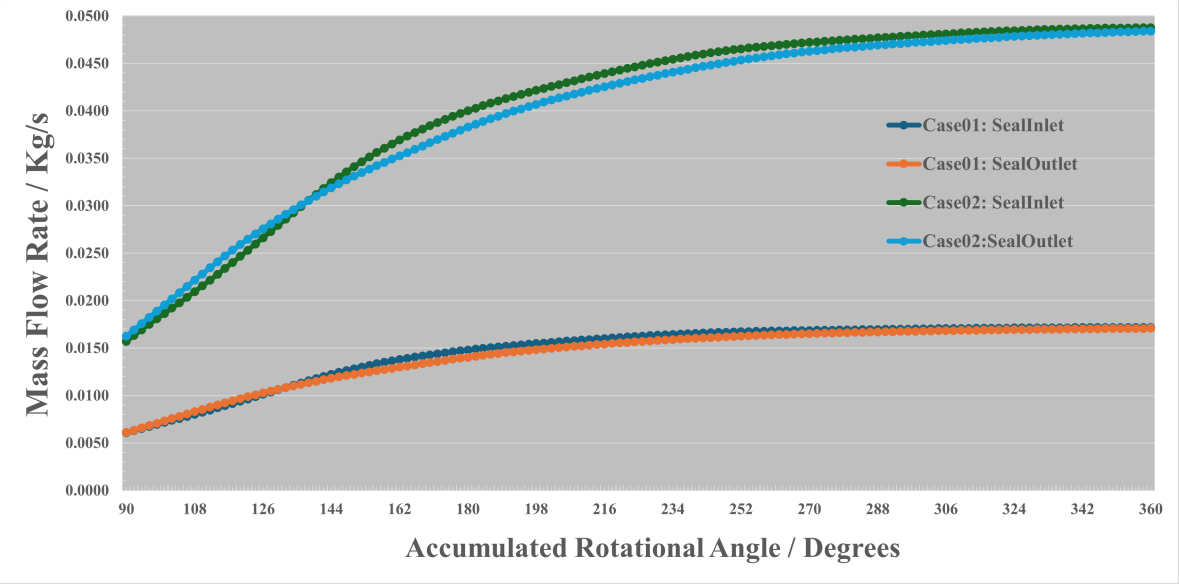

Figure 5.8: Inlet and outlet mass flows of gap seals for Case01 and Case02 starting from rotational position of 90 degrees.

Volumetric efficiency and compressor power consumption (P_{comp}) are two main parameters reflecting the capacity and practicality of the compressor models built in this research with gap seals. These values, with different ψ, are compared with Marina's model, as shown in Figure 5.9. Furthermore, the percentage difference of each term between the two models is recorded in Table 5.8. From the graph, it is clear that both values follow the same developmental trend, with the maximum percentage difference being approximately 6.35%. The overall error range is in line with expectations. Consequently, it can be concluded that the addition of a gap seal up to 40% seal mass

fraction does not significantly lower efficiency and power consumption, with the formula for power consumption given in Eq.5.5, where τ is the torque of the rotor.

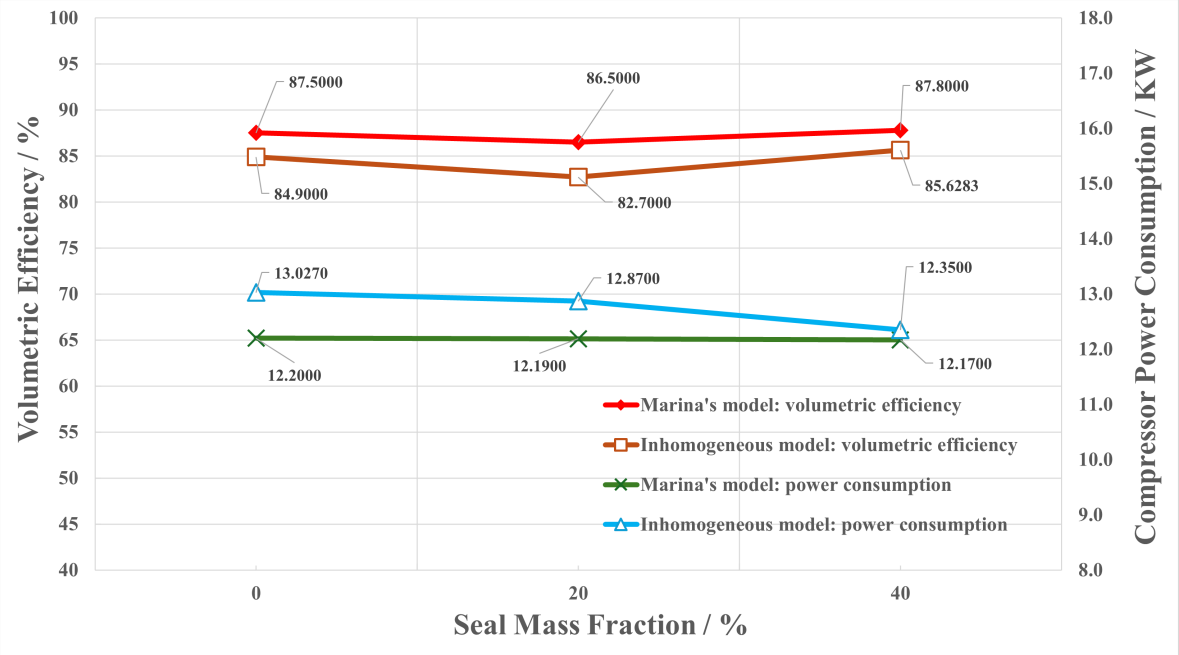

Figure 5.9: Volumetric efficiency and power consumption of the compressor built with gap seals. Results are compared with Marina's model.

Table 5.8: The percentage differences between the models of this research and Marina's for volumetric efficiency and power consumption in each case.

Term	Case01	Case02	Case03
Volumetric efficiency (%)	2.97	4.39	2.47
Power consumption (%)	6.35	5.28	1.46

$$P_{comp} = \tau_{rotor1} \cdot \Omega_{rotor1} + \tau_{rotor2} \cdot \Omega_{rotor2} \tag{5.5}$$

The addition of gap seals improves the mixing of seal and suction mass flows, boosting local velocity, as shown in Figures 5.10 and 5.11. When multiphase flow enters the gap seal, its velocity abruptly increases due to rapid channel volume reduction. As the flow is pumped up, velocity decreases slightly due to gravity before increasing rapidly near the lower-pressure seal outlet. At the 90-degree rotational position, flow inside

the suction domain in Figure 5.10 is well mixed, unlike the layered flow in Figure 5.11. Consequently, high-velocity gap seal flows enhance flow transportation from the suction domain to the rotor, preparing it for compression. However, due to the small inter-lobe and rotor tip clearances, the volume of flow entering the rotor remains largely unchanged, resulting in similar velocity contours in both compression domains.

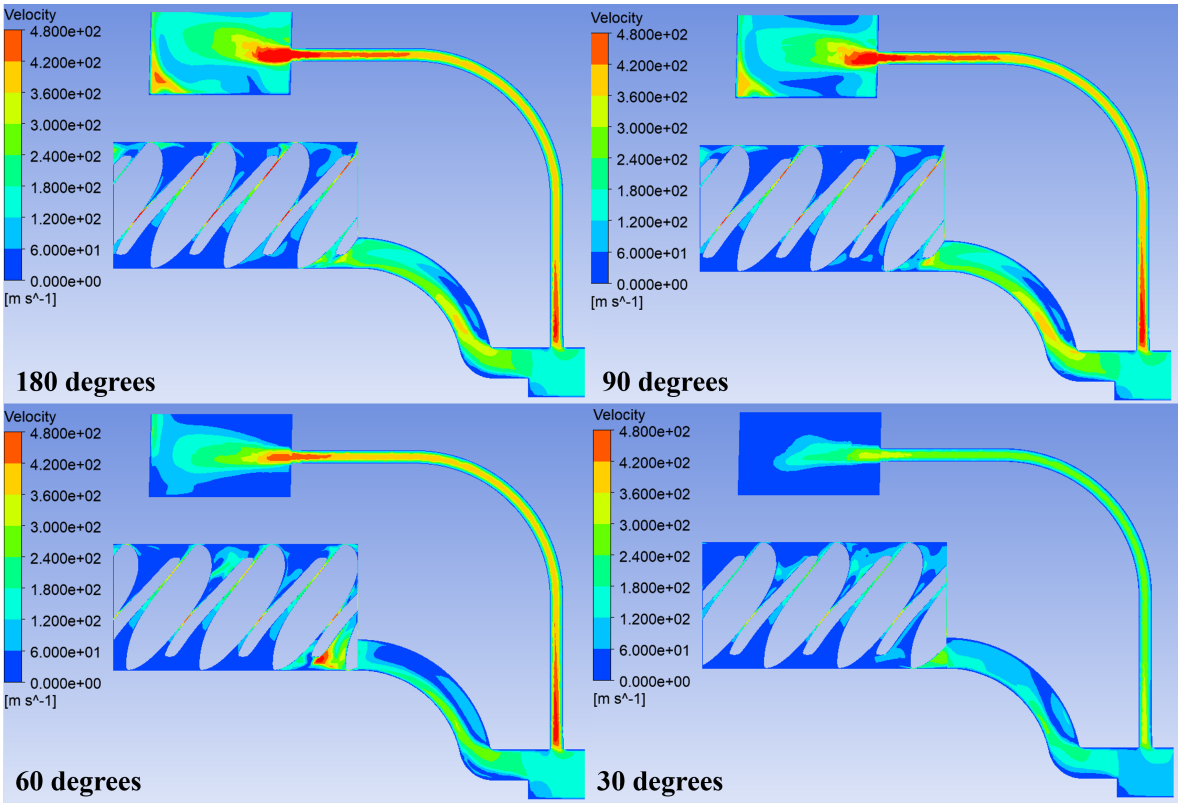

Figure 5.10: The contour of global velocity distribution for Case02 with gap seals.

After the $80th$ time step, corresponding to 160 degrees, the pressure distribution at both the discharge outlet and the maximum point in the discharge domain becomes stable and periodic, as shown in Figure 5.12. This indicates that the excessive velocity at the rotor inlet due to the addition of gap seals does not adversely affect the pressurization process, ensuring it is not a potential issue for compressor performance. Therefore, it is recommended to add such channels to help alleviate internal leakage, mix the suction flow well, and ensure sufficient and stable pressurization. Last, volume fractions for the mixture is shown in Figure 5.13.

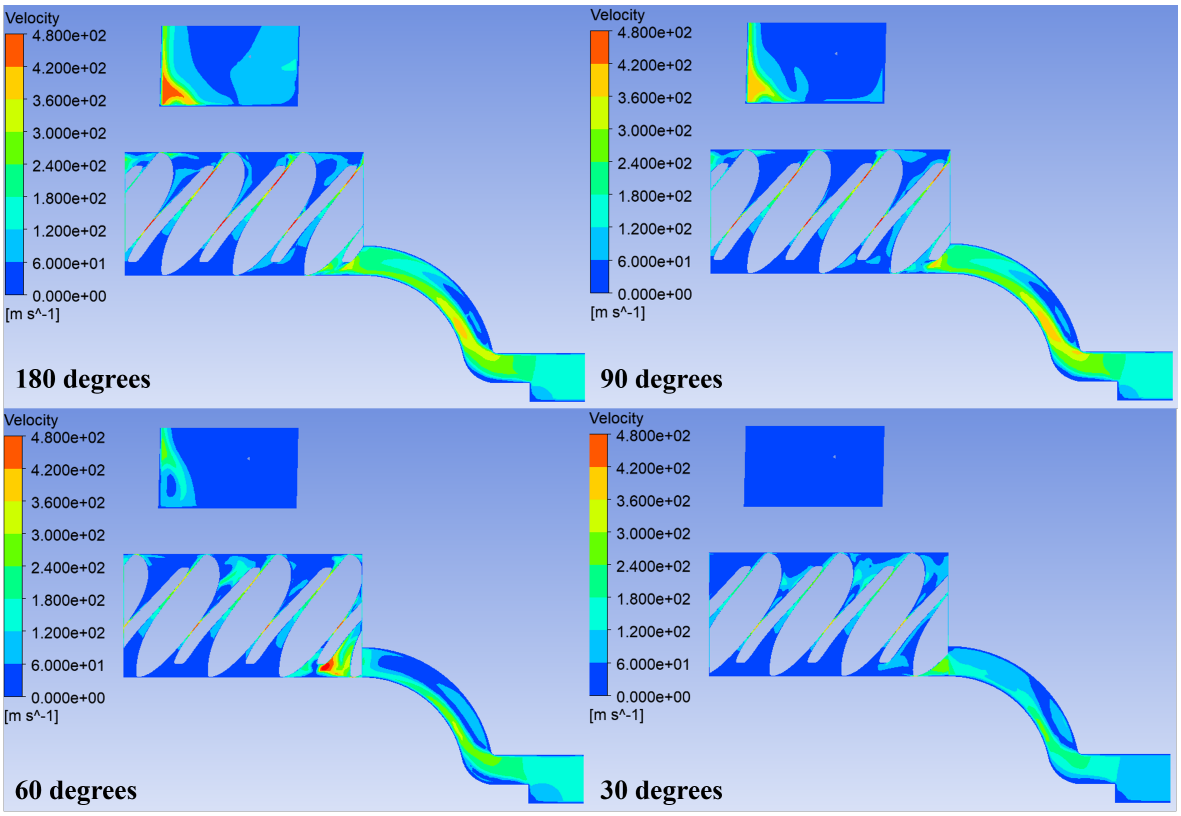

Figure 5.11: The contour of global velocity distribution for Case01 without gap seals.

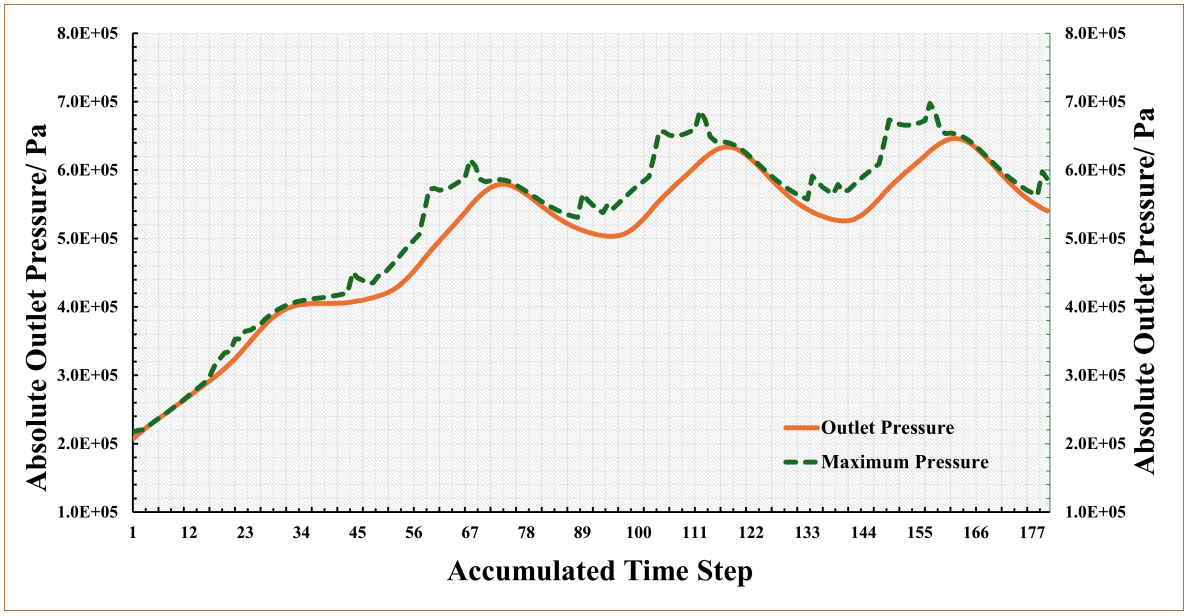

Figure 5.12: The curve of outlet and maximum pressure distribution for Case02 with gap seals.

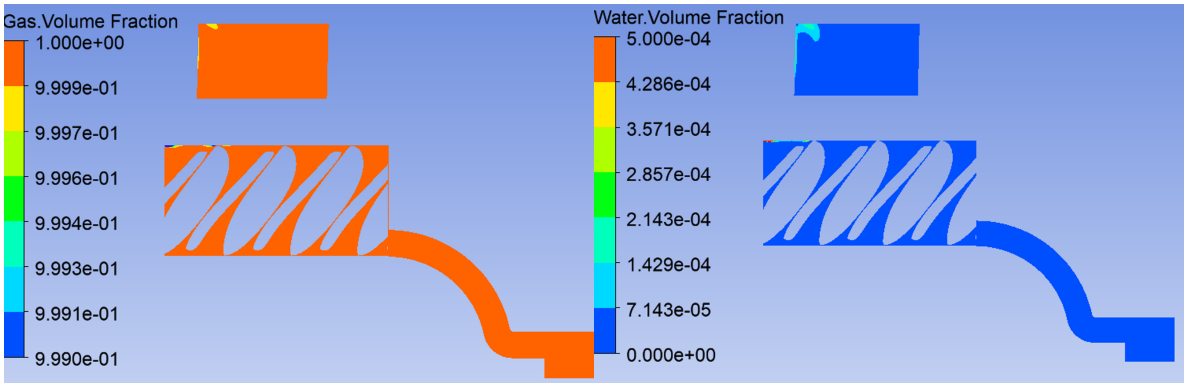

Figure 5.13: The contours of volume fraction demonstrations for the mixture with gap seals added.

Chapter 6

Conclusions

This research focuses on the numerical simulation of ideal single-phase airflow and multi-phase ammonia-water flows within twin-screw compressors. The primary challenge lies in accurately modeling the pressurization processes as fluid flows through narrow passages. These passages include the irregular and sinuous clearances between male and female rotor tips and the small spaces between the rotors and the stator's inner walls. This requires advanced techniques in both modeling and meshing. The model, developed and refined in Inventor, omits secondary components such as bearings and elastic washers but captures the screw and chamber features effectively. To enhance sealing and pressurization, the rotor tip and inter-lobe clearances are minimized, avoiding negative volume and excessive pressure pulsation within the enclosed cavity.

The stator mesh was initially created in Fluent Meshing using the SST method, achieving high orthogonal quality, aspect ratio, and skewness. However, after recognizing that TwinMesh is more effective at handling complex rotor meshing challenges, such as adaptability and numerical stability in dynamic mesh deformation, Ansys Meshing was used to regenerate the stator grid due to its better compatibility with TwinMesh. While the three evaluation parameters in Ansys Meshing perform slightly lower than in Fluent Meshing, they still meet the required standards. TwinMesh employs a two-step meshing strategy for the screw and axial gap domains of the male and female rotors,

effectively accounting for axial gap flow. The minimum orthogonal angle of 18 degrees and maximum aspect ratio of 1000 are met in all eight mesh cases, except for Mesh05, which has too few circumferential nodes.

An ideal single-phase airflow simulation was conducted to validate the model's reliability, with conservation laws of mass, momentum, total energy, geometry, and turbulence enclosure properly set. A high-resolution advection scheme and second-order backward Euler transient scheme were selected, with opening boundary conditions accounting for backflow. The mesh independence study shows that increasing the maximum element size from 1 mm to 1.4 mm maintains grid refinement accuracy, while an oversized selection like 2 mm coarsens and deteriorates the mesh. The optimal range for circumferential node count is between 160 and 360, with Mesh01 and Mesh07 having 200 nodes performing best. Excessive nodes lead to large aspect ratios, while too few coarsen the grid and reduce spatial resolution. Obvious periodic pressure variations were recorded in snapshots of the global pressure distribution at each 15-degree rotation. The outlet pressure first reaches the target value at 90 degrees and recurs every 90 degrees. The peak pressure is approximately 3.2 bar, 6% higher than the 3-bar setting. These high-amplitude pressure fluctuations at the outlet are unfavorable for the compressor and should be controlled to avoid excessive pressure pulsation. Installing a PID controller, frequency converter, or adopting a multi-stage compressor design can effectively address this issue. Additionally, the temperature in the simulations increases to around 125°C, starting from an inlet temperature of 25°C, which could cause thermal stress and material fatigue. Therefore, an ammonia-water multiphase compression process with wet compression was implemented to control the outlet temperature.

The introduction of the phase boundary complicates mesh generation, as high gradients at element vertices can cause solutions to diverge. TwinMesh addresses this with new strategies, including halved mesh density per pitch angle, Type 2 interface generation, and the Outerfix meshing type. The mesh independence study focuses on radial divisions, angular resolution, and axial divisions. Increasing radial divisions has minimal impact on mesh quality. Adjusting angular resolution to 2 degrees balances

accuracy and computational resources. Sampling is needed to compare variables, as different angular resolutions lead to varying rotational positions. Axial division, typically set by wrap angle and angular resolution, was intentionally reduced in Mesh06 to assess its impact. Significant deviations, especially in mass flow, were observed. Furthermore, water droplet diameters were determined using the SMD method, assuming constant water density during compression for simplicity. The 10-micron size is much smaller than the narrowest points in the screw domains, ensuring smooth fluid flow.

The homogeneous model was developed for a mesh independence study of multi-phase flows, while the inhomogeneous particle model was introduced for a more accurate representation of the pressurization process. The inhomogeneous model separately treats the governing equations for continuous ammonia vapor and discrete water droplets, using a dispersed phase zero-equation model in place of the SST model for droplet turbulence. Compared to Kathari's experimental data on volumetric efficiency, the homogeneous model shows a maximum deviation of 19.8% across three rotational speeds, while the inhomogeneous model's largest deviation is only 8.9%. Additionally, with identical inlet temperature and pressure to single-phase flow, the outlet temperature from the inhomogeneous multi-phase model is 112°C, roughly 10% lower, indicating that wet compression effectively controls temperature rise. To account for external leakage inside compressors from the discharge to the suction domain, gap seals were implemented to facilitate backflow. Overall, inlet and outlet mass flows remain balanced for both the global fluid domains and the gap seal, and volumetric efficiency and power consumption are similar to models without the seal. Pressure contour snapshots at 30, 60, 90, and 180 degrees show high-speed fluid from the gap seal outlet merging well with the suction domain flow, enhancing its transfer to the screw domain. Consequently, the addition of a gap seal improves circulation and pressurization while maintaining performance of the compressor.

Bibliography

[1] N. Gregory Mankiw. *Principles of macroeconomics*. Mason, OH : South-Western Cengage Learning, 2012.

[2] World Bank. *The World Bank Annual Report 2022*. The World Bank, 2022.

[3] Jing Zhang, Hong-Hu Zhang, Ya-Ling He, and Wen-Quan Tao. A comprehensive review on advances and applications of industrial heat pumps based on the practices in china. *Applied Energy*, 178:800–825, 2016.

[4] Paúl Dávila, Mahmoud Bourouis, Juan Francisco Nicolalde, and Javier Martínez-Gómez. Modelling and analysis of a compression/resorption heat pump system with a zeotropic mixture of acetone/co2. *Applied Thermal Engineering*, 227:120388, 2023.

[5] Natasa Markovska, Neven Duić, Brian Vad Mathiesen, Zvonimir Guzović, Antonio Piacentino, Holger Schlör, and Henrik Lund. Addressing the main challenges of energy security in the twenty-first century – contributions of the conferences on sustainable development of energy, water and environment systems. *Energy*, 115:1504–1512, 2016. Sustainable Development of Energy, Water and Environment Systems.

[6] Yun Gao. China's response to climate change issues after paris climate change conference. *Advances in Climate Change Research*, 7(4):235–240, 2016. Including special topic on Sino-India monitor on NDCs.

[7] Muhammad Salman, Xingle Long, Guimei Wang, and Donglan Zha. Paris climate agreement and global environmental efficiency: New evidence from fuzzy regression discontinuity design. *Energy Policy*, 168:113128, 2022.

[8] Anton A Kiss and Carlos A Infante Ferreira. *Heat pumps in chemical process industry*. CRC Press, 2016.

[9] Benjamin Zühlsdorf, Jonas Kjær Jensen, Stefano Cignitti, Claus Madsen, and Brian Elmegaard. Analysis of temperature glide matching of heat pumps with zeotropic working fluid mixtures for different temperature glides. *Energy*, 153:650–660, 2018.

[10] Anton A. Kiss, Servando J. Flores Landaeta, and Carlos A. Infante Ferreira. Towards energy efficient distillation technologies – making the right choice. *Energy*, 47(1):531–542, 2012. Asia-Pacific Forum on Renewable Energy 2011.

[11] Hao Luo, Costin Sorin Bildea, and Anton A. Kiss. Novel heat-pump-assisted extractive distillation for bioethanol purification. *Industrial & Engineering Chemistry Research*, 54(7):2208–2213, 2015.

[12] Hossein Shahandeh, Mina Jafari, Norollah Kasiri, and Javad Ivakpour. Economic optimization of heat pump-assisted distillation columns in methanol-water separation. *Energy*, 80:496–508, 2015.

[13] Nguyen Van Duc Long and Moonyong Lee. A hybrid technology combining heat pump and thermally coupled distillation sequence for retrofit and debottlenecking. *Energy*, 81:103–110, 2015.

[14] Miguel A Navarro-Amorós, Rubén Ruiz-Femenia, and José A Caballero. A new technique for recovering energy in thermally coupled distillation using vapor recompression cycles. *AIChE Journal*, 59(10):3767–3781, 2013.

[15] D.M. van de Bor, C.A. Infante Ferreira, and Anton A. Kiss. Optimal performance of compression–resorption heat pump systems. *Applied Thermal Engineering*, 65(1):219–225, 2014.

[16] Michel D. Obrist, Ramachandran Kannan, Russell McKenna, Thomas J. Schmidt, and Tom Kober. High-temperature heat pumps in climate pathways for selected industry sectors in switzerland. *Energy Policy*, 173:113383, 2023.

[17] IEA. *Application of Industrial Heat Pumps*. Technical report, 2014.

[18] V. Gudjonsdottir and C.A. Infante Ferreira. Technical and economic analysis of wet compression–resorption heat pumps. *International Journal of Refrigeration*, 117:140–149, 2020.

[19] Cordin Arpagaus, Frédéric Bless, Michael Uhlmann, Jürg Schiffmann, and Stefan S. Bertsch. High temperature heat pumps: Market overview, state of the art, research status, refrigerants, and application potentials. *Energy*, 152:985–1010, 2018.

[20] Experimental performance of high temperature heat pump with near-azeotropic refrigerant mixture. *Energy and Buildings*, 78:43–49, 2014.

[21] Yan Zhang, Yufeng Zhang, Xiaohui Yu, Jing Guo, Na Deng, Shengming Dong, Zhonglu He, and Xuelian Ma. Analysis of a high temperature heat pump using by-5 as refrigerant. *Applied Thermal Engineering*, 127:1461–1468, 2017.

[22] D.M. van de Bor, C.A. Infante Ferreira, and Anton A. Kiss. Low grade waste heat recovery using heat pumps and power cycles. *Energy*, 89:864–873, 2015.

[23] V. Gudjonsdottir, C.A. Infante Ferreira, Glenn Rexwinkel, and Anton A. Kiss. Enhanced performance of wet compression-resorption heat pumps by using nh3-co2-h2o as working fluid. *Energy*, 124:531–542, 2017.

[24] Qun Zheng, Yufeng Sun, Shuying Li, and Yunhui Wang. Thermodynamic Analyses of Wet Compression Process in the Compressor of Gas Turbine . *Journal of Turbomachinery*, 125(3):489–496, 2003.

[25] Sepehr Sanaye and Mojtaba Tahani. Analysis of gas turbine operating parameters with inlet fogging and wet compression processes. *Applied Thermal Engineering*, 30(2):234–244, 2010.

[26] The wet compression technology for gas turbine power plants: Thermodynamic model. *Applied Thermal Engineering*, 27(4):699–704, 2007. Energy: Production, Distribution and Conservation.

[27] Abhay Mohan, Palani Kumar Chidambaram, Abhilash Suryan, and Heuy Dong Kim. Energy efficiency analysis of wet compression systems through thermo-fluid dynamic considerations. *Journal of Cleaner Production*, 214:132–144, 2019.

[28] P. V. Hudson Dharmaraj, T. H. Kim, A. Suryan, and H. D. Kim. Thermo-fluid analysis on the efficiency of wet compression process. *Journal of Applied Fluid Mechanics*, 15(4):1061–1071, 2022.

[29] Jianting Sun, Zhitao Zuo, Qi Liang, Xuehui Zhang, Huan Guo, and Haisheng Chen. Theoretical and experimental study on effects of wet compression on centrifugal compressor performance. *Applied Thermal Engineering*, 212:118163, 2022.

[30] P.P.J Vorster and J.P Meyer. Wet compression versus dry compression in heat pumps working with pure refrigerants or non-azeotropic binary mixtures for different heating applications. *International Journal of Refrigeration*, 23(4):292–311, 2000.

[31] L.C.M Itard. Wet compression versus dry compression in heat pumps working with pure refrigerants or non-azeotropic mixtures. *International Journal of Refrigeration*, 18(7):495–504, 1995.

[32] Shizhong Sun, Ziwen Xing, Yanpeng Li, Po Chia Su, and Wenqing Chen. Experimental investigation on twin screw refrigeration compressor with different capacity control methods. *International Journal of Refrigeration*, 130:370–381, 2021.

[33] Feng Cao, Tieyu Gao, Songshan Li, Ziwen Xing, and Pengcheng Shu. Experimental analysis of pressure distribution in a twin screw compressor for multiphase duties. *Experimental Thermal and Fluid Science*, 35(1):219–225, 2011.

[34] Xueyuan Peng, Ziwen Xing, Tiansheng Cui, and Liansheng Li. Analysis of the working process in an oil-flooded screw compressor by means of an indicator diagram. *Proceedings of the Institution of Mechanical Engineers, Part A: Journal of Power and Energy*, 216(6):465–470, 2002.

[35] Bingqi Wang, Xiaokun Wu, Chuang Wang, Zhiping Zhang, Shizhong Sun, and Ziwen Xing. Study on non-uniform internal pressure distribution of twin-screw refrigeration compressor. *International Journal of Refrigeration*, 152:214–222, 2023.

[36] Bingqi Wang, Xiaokun Wu, Chuang Wang, Zhiping Zhang, Yuchen Li, and Ziwen Xing. Performance improvement of twin screw refrigeration compressors for chillers by modifying the suction arrangement. *International Journal of Refrigeration*, 2023.

[37] Shizhong Sun, Xiaokun Wu, Dantong Li, Chuang Wang, and Ziwen Xing. Study on suction pressure loss near suction end and stagnant pressure rise in p- diagram of twin-screw refrigeration compressor for chiller. *Thermal Science and Engineering Progress*, 34:101410, 2022.

[38] Shengmei Yang, Hua Ouyang, Yadong Wu, Lee Wang, Lu Mei, and Hongdan Wang. Cfd simulation for the internal pressure characteristics of an oil-injected twin-screw refrigeration compressor. *International Journal of Refrigeration*, 126:143–154, 2021.

[39] S. Rane, A. Kovacevic, N. Stosic, and M. Kethidi. Cfd grid generation and analysis of screw compressor with variable geometry rotors. In *8th International Conference on Compressors and their Systems*, pages 601–612. Woodhead Publishing, 2013.

[40] Sham Rane, Ahmed Kovacevic, Nikola Stosic, and Madhulika Kethidi. Deforming grid generation and cfd analysis of variable geometry screw compressors. *Computers Fluids*, 99:124–141, 2014.

[41] Sham Rane, Ahmed Kovacevic, Nikola Stosic, and Madhulika Kethidi. Grid deformation strategies for cfd analysis of screw compressors. *International Journal of Refrigeration*, 36(7):1883–1893, 2013. New Developments in Compressor Technology.

[42] Sham Rane, Ahmed Kovačević, Nikola Stošić, and Ian Smith. Analysis of real gas equation of state for cfd modelling of twin screw expanders with r245fa, r290, r1336mzz(z) and r1233zd(e). *International Journal of Refrigeration*, 121:313–326, 2021.

[43] A Kovacevic, M Kethidi, N Stosic, E Mujic, and IK Smith. „turbulence capture in cfd for screw machines,“. *Schraubenmaschinen 2010*, pages 245–260, 2010.

[44] Huagen Wu, Kanlong Lin, Hao Huang, Baoshun Xiong, Beiyu Zhang, and Ziwen Xing. Research on effects of vapor injection on twin-screw compressor performance. *International Journal of Refrigeration*, 118:483–490, 2020.

[45] Nausheen Basha, Ahmed Kovacevic, and Sham Rane. Numerical investigation of oil injection in screw compressors. *Applied Thermal Engineering*, 193:116959, 2021.

[46] Wei Yang, Yong Quan, Xinyang Jin, Yukio Tamura, and Ming Gu. Influences of equilibrium atmosphere boundary layer and turbulence parameter on wind loads of low-rise buildings. *Journal of Wind Engineering and Industrial Aerodynamics*, 96(10):2080–2092, 2008. 4th International Symposium on Computational Wind Engineering (CWE2006).

[47] Konstantinos Vontas, Marco Pavarani, Nicolas Miché, Marco Marengo, and Anastasios Georgoulas. Validation of the eulerian–eulerian two-fluid method and the rpi wall partitioning model predictions in openfoam with respect to the flow boiling

characteristics within conventional tubes and micro-channels. *Energies*, 16(13), 2023.

[48] C. Gómez-Zarzuela, C. Peña-Monferrer, S. Chiva, and R. Miró. Development and validation of a one-dimensional solver in a cfd platform for boiling flows in bubbly regimes. *Progress in Nuclear Energy*, 134:103680, 2021.

[49] VV Kothari. Experimental validation of wet compression with a twin screw compressor prototype. 2020.